Department of Precision and Microsystems Engineering

Optimizing Nanomechanical Resonators

Hendrik Jaap Algra

Report no : 2024.013
Coach : Z. Li
Professor : dr. F. Alijani & dr. A.M. Aragón
Specialization : DMN & CDM
Type of report : Master Thesis
Date : 20 February 2024

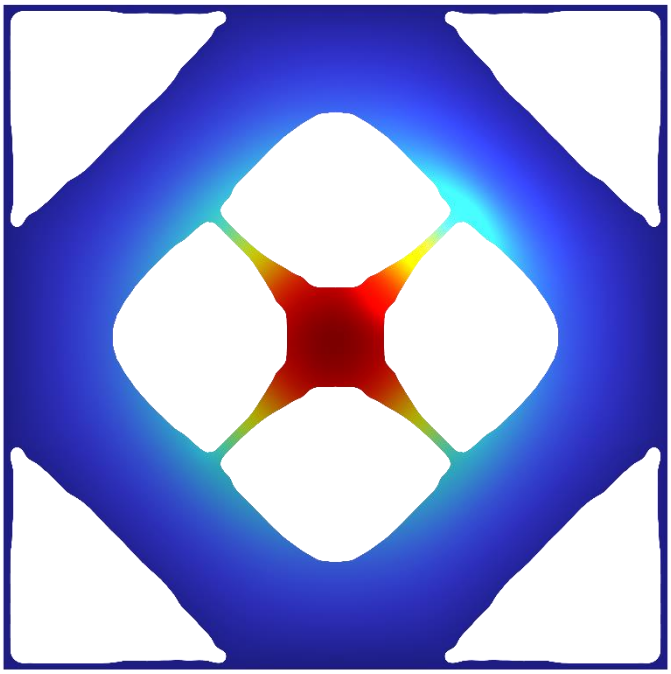

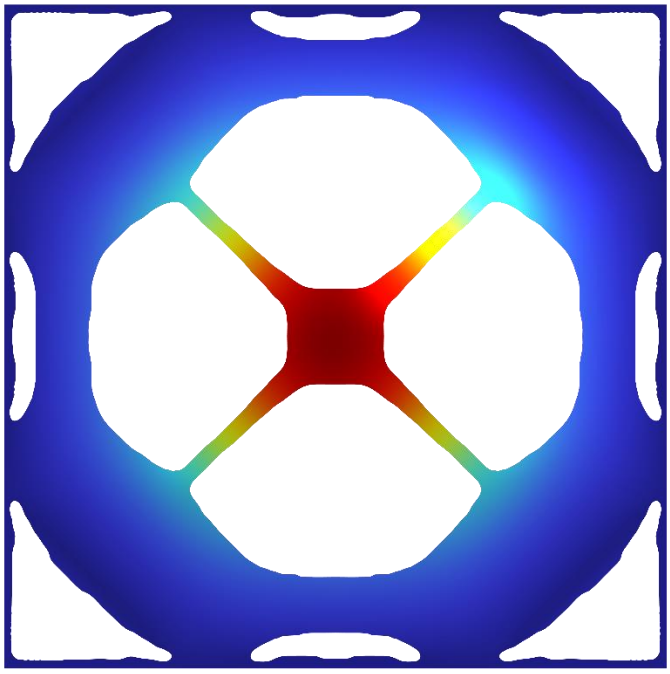

TU Delft Delft University of Technology

Challenge the future

Optimizing Nanomechanical Resonators

MSc. Thesis

H.J. Algra

Student Name	Student Number
Hendrik Jaap Algra	5654890

DMN Professor:	dr. F. Alijani
CDM Professor :	dr. A.M. Aragón
Daily Supervisor:	Z. Li
Project Duration:	February, 2023 - February, 2024
Faculty:	Mechanical Engineering

A digital version of this thesis is available at https://repository.tudelft.nl
Note : This work is under embargo until March 1, 2026.

TU Delft

Preface

This work concludes my journey towards obtaining a Master of Science degree in mechanical engineering at Delft University of Technology. In this short preface, I would like to express my gratitude towards my direct supervisors, Farbod, Alejandro, and Zichao for their guidance during this project. I can truly say that I have learned a lot during the past year, and feel blessed to have worked with you as my supervisors.

Furthermore, I would like to express my thanks to other staff members Fred, Matthijs and Surya for making time to meet with me and discuss difficulties that arose over the course of my project.

Last but not least, I would like to emphasize my gratitude towards my friends and family who have supported me throughout my life.

H.J. Algra
Delft, February 2024

Contents

Preface i

Nomenclature iii

1 Introduction 1

2 Literature Review 2
- 2.1 Dissipation Mechanisms . . . 2
- 2.2 Dissipation Dilution . . . 3
- 2.3 High-Q Resonator Designs . . . 3
- 2.4 Optimization for Q factors . . . 4
- 2.5 Conclusion & Research Gap . . . 5

3 Topology Optimization for Improving Dissipation Dilution in Nanomechanical Resonators 7

4 Nelson's Method for Computing Prestressed Eigenvector Gradients 22

5 Conclusion & Outlook 27

References 29

A Project Time Management 32

B Contributions To `Hybrida` 34

C Guide to Working with `Hybrida` on Windows 37

Nomenclature

Abbreviations

Abbreviation	Definition
FEA / FEM	Finite Element Analysis / Method
TO	Topology Optimization

Symbols

Symbol	Definition	Unit
f_0	Fundamental eigenfrequency	[Hz]
ω	Eigenfrequency	[rad/s]
ρ_e	Design density	
$\tilde{\rho}_e$	Filtered density	
$\bar{\rho}_e$	Projected density	
$\boldsymbol{S}$	Elasticity matrix	[Pa]
$\boldsymbol{D}$	Linear strain-displacement matrix	[1/m]
$\boldsymbol{\sigma}_0$	Prestress vector	[Pa]
$\boldsymbol{f}_\sigma$	Prestress contribution to force vector	[N]
$\boldsymbol{K}$	Linear stiffness matrix	[N/m]
$\boldsymbol{u}_\sigma$	Static displacement	[m]
$\boldsymbol{G}$	Geometric stiffness matrix	[N/m]
$\boldsymbol{M}$	Mass matrix	[kg]
$\boldsymbol{\phi}$	Mode shape	

1 Introduction

Precise measurements of physical quantities such as mass and acceleration are integrated into our daily lives. On a daily basis, people measure the weight of objects around them, such as fruits and vegetables in the supermarket, or even themselves when stepping onto a scale. Our smartphones employ accelerometers to record the number of steps we take, and in some cases they can even detect the occurrence of severe car crashes [1]. To conduct similar measurements on the nanoscale, so-called *nanomechanical resonators* can be used. These devices are designed to oscillate at a specific resonance frequency, and have dimensions ranging from one down to a thousandth's times the thickness of a human hair. A critical property of certain *"High-Q"* resonators is their extremely low energy dissipation rate, resulting in an elongated ringdown time. This feature has attracted a considerable amount of attention over the past decades, as it allows them to be used as force sensors [2], mass sensors [3, 4] and for fundamental studies in the quantum regime [5, 6].

When these resonators are used as a measurement probe, a limiting factor to their accuracy (and therefore their usefulness) is the influence of thermal noise, which exerts a random force on the oscillating body [7]. This thermal noise force limits the precision with which quantities such as forces, masses or pressures can be detected [8]. From the fluctuation-dissipation theorem, it is known that the influence of thermal noise increases with resonator mass, temperature and dissipation rate [7]. Apart from reducing the mass and operation temperature of these oscillators, minimizing the amount of energy they dissipate is a critical aspect of thermal noise mitigation [9]. A low dissipation rate has several other benefits which include (but are not limited to) the enabling of the oscillator to function at low power and a sharper resonance peak (which allows the resonance frequency of the oscillator to be determined more accurately) [10]. An important figure of merit coined as the *Quality Factor* (Q factor) is inversely related to the dissipation rate of an oscillator, and is commonly used to quantify the performance of a resonator design. One of the most important aspects that influences a resonator's Q factor is its geometry. Studies looking into this dependency have resulted in wide variety of resonator designs, which all aim to achieve an extremely high Q factor. However, the driving force behind the majority of high-Q designs has been human intuition. Only a handful of studies have looked into applying (structural) optimization techniques to design resonators with extremely high Q factors (e.g., [8] and [11]). However, to the author's best knowledge, no studies exist that employ topology optimization techniques (in this context) that do not require *a priori* knowledge from the user.

The goal of this thesis is therefore to investigate and apply structural optimization techniques to maximize the Q factor of nanomechanical structures. It commences in Chapter 2 with a brief literature review, giving an overview of structural damping mechanisms as well as high-Q resonator designs used to mitigate them. Furthermore, it gives examples of how optimization techniques have been applied to design geometries with increasingly higher Q factors. This is succeeded by the main work of this project, which is written in the form of a manuscript in Chapter 3. An additional manuscript given in Chapter 4 describes a novel idea concerning Lagrange multipliers that was looked into. The thesis concludes with a discussion and an outlook in Chapter 5.

2

Literature Review

This chapter concisely describes a handful of fundamental principles associated with the Q factor of nanomechanical resonators, such as damping mechanisms as well as the role of (pre)stress. Furthermore, it highlights a few prominent resonator designs used to achieve extremely high Q factors, including their advantages and drawbacks.

2.1. Dissipation Mechanisms

When allowed to oscillate freely, the vibration amplitude of any resonator will slowly decay due to a variety of dissipation mechanisms. The Q factor is a measure of this decay rate, as it is inversely proportional to the amount of energy lost per oscillation. The most important dissipative effects in high-Q resonators can be roughly divided into three categories [12], which are discussed below.

- **Medium damping** is a ubiquitous source of dissipation and describes the interaction between the vibrating structure and the surrounding gas molecules. To mitigate this effect, resonators are commonly operated in a vacuum chamber. At very low pressures, interactions with surrounding molecules still result in energy dissipation [13], but are assumed to be negligible compared to other sources of damping [14]. Certain applications such as microchannel resonators, which are used to measure the weight of biological molecules [15], also experience medium damping originating from an internal viscous fluid, but these are not of interest for this project.
- **Acoustic Clamping Losses** are caused by *phonons*, waves of elastic energy that can radiate out of the resonator into the surrounding substrate. The magnitude of this loss mechanism strongly depends on the geometry of the resonator, as well as the amount of tension which increases the coupling to the substrate [10]. It has been shown that the lower vibration modes are especially sensitive to the way in which the resonator is mounted to its substrate, and that the acoustic loss can be reduced by minimizing contact between the resonator and its support. Furthermore, for higher order modes this damping mechanism can effectively be alleviated by using a *phononic crystal*, which is a structure that prevents phonons of certain frequencies from passing [16, 17]. In general, the following scaling law has been observed for singly and doubly-clamped beams of which the Q factor is limited by acoustic radiation as $Q_{acoustic} \propto L/w$, where L and w denote the length and width of the resonator. In resonators in which this damping mechanism is not dominant, the scaling of Q with geometric parameters can be different [9, 10].
- **Intrinsic Damping** describes all dissipative effects inherent to the surface or inner bulk of vibrating material. A fundamental effect that belongs to this category is the internal friction caused by a phase difference φ between the stress and (lagging) strain fields [14, 18, 19]. Energy losses occur as the strain moves toward a new equilibrium, and can primarily be attributed to local strain variations (as global elongations generally have a negligible contribution to this mechanism) [12]. The Q factor of resonators that are limited by this intrinsic damping mechanism can be calculated using only the aforementioned phase difference φ, by means of the relation $Q_{int} \approx 1/\varphi$. Finally, resonators experience certain intrinsic loss mechanisms that cannot be completely cir-

cumvented (known as *fundamental losses*), which pose a theoretical upper limit to the maximum Q factor or $Q \times f_0$ product. Both the varying strain field (*thermo-elastic damping*) as well as the interaction between phonons (*the Alkhiezer effect* [20]) lead to irreversible heat flow within a structure. Although the effects of thermo-elastic damping are reduced at lower temperatures, and the Alkhiezer effect only becomes important in the higher GHz range, all resonators are ultimately limited by these effects and inevitably show an inverse scaling between their Q factors and their resonance frequency [21].

2.2. Dissipation Dilution

The presence of static stress in membranes or beams is commonly observed to coincide with an increase of the quality factor of their vibration modes. This effect, known as *dissipation dilution* [22, 23], has been extensively researched during the past decade. A simple way of describing this effect is the reduction of intrinsic dissipation (for certain flexural modes) in the presence of stress [24]. The energy stored inside a resonating structure under stress can be divided into two components, namely "tensile" and "bending" energies. The tensile energy stored in the structure acts as a lossless potential, increases stiffness without adding loss [22, 23, 25]. As the geometry of the resonator strongly influence on this phenomenon, its structural design offers researchers a way to enhance Q factors.

2.3. High-Q Resonator Designs

For sensing applications and quantum experiments alike, a wide range of studies have been conducted over the years aiming to design resonators with ever-increasing Q factors. A well-established approach which underlies many designs is the identification of a certain damping mechanism alongside design principles that aim to mitigate energy dissipation via the respective mechanism.

Fractal-Shaped Resonators

An important side effect of increasing the tensile stress in resonators is an associated increase in material friction losses at the clamping sites, caused by a higher local bending curvature. This limits the effects of dissipation dilution [26]. In order to reduce these losses, resonators can be designed to be *softly-clamped*. This means that the curvature of the mode shape is strongly reduced whilst stress is preserved near the clamping sites. Certain "fractal-like" resonators were designed to employ this principle [18, 25], as example of which can be found in Figure 2.1. In this design, the gradient of the vibration amplitude was found to decrease by a factor of $\cos\alpha$ as the mode passed over each branching point (with α indicating the outward angle between the subsequent branches). The optimal value of α was found to be slightly below $\pi/2$, due to an associated increase in torsional bending losses as the angle became orthogonal.

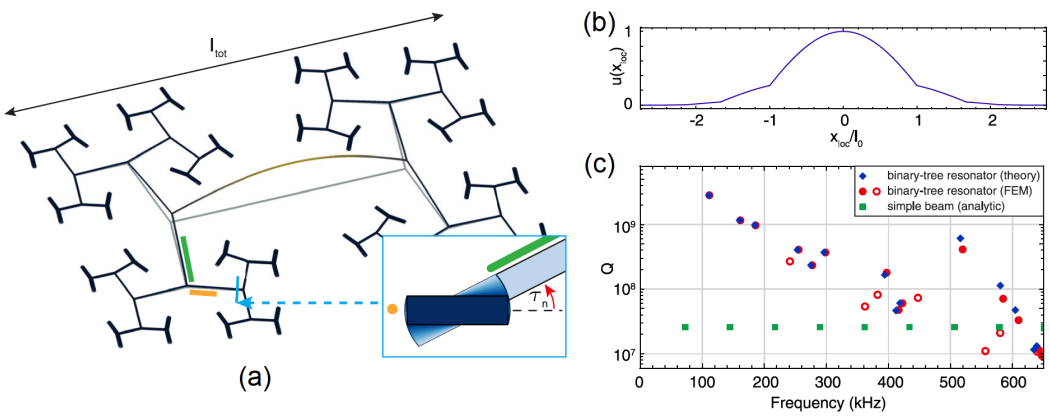

Figure 2.1: (a) Fundamental mode of the branched hierarchical resonator structure, showing torsional deformation at the branching site in the cutout. (b) Associated normalized displacement, following a path from the center of the longest beam to one of the clamping sites (c). Analytical and numerical Q factors and frequencies of this structure, compared to those of a doubly clamped beam resonator of the same length. Adapted from [7].

Phononic Crystal Structures

In order to reduce the energy dissipation via acoustic radiation, phononic crystal structures can be engineering in beams [27] or membranes [24], which confine a (higher order) mode to the center of the vibrating structure. An illustrative example of such a structure and its effects can be found in Figure 2.2. Although phononic crystals can be used to design structures with Q factors close to the limit set by fundamental losses [28], they always target a certain higher-order mode. For practical sensing applications as well as quantum experiments, the fundamental mode is of interest as higher-order modes are more difficult to observe and can be affected by neighboring modes [6, 26]. Another downside to this structure is the difficulty of reliable fabrication, which is further complicated by the fact that significant mode localization requires the device to be much larger than the mode shape of interest [8, 26].

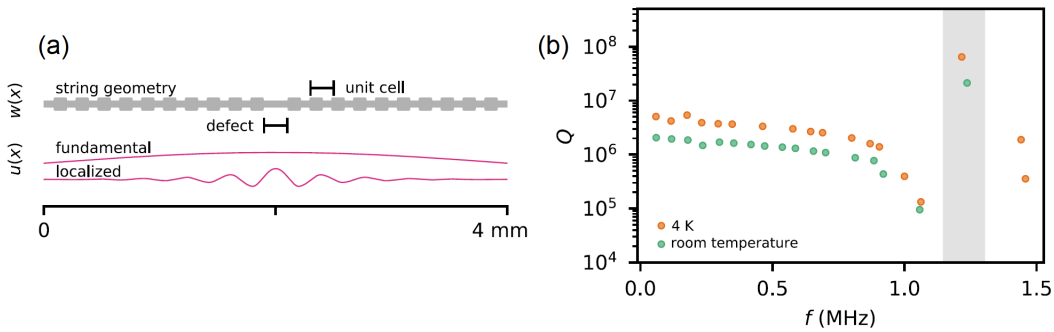

Figure 2.2: (a) A string resonator with a geometric design resulting in a phononic bandgap (width depicted by $w(x)$), with the fundamental and localized mode shapes of the structure (displacement depicted by $u(x)$).
(b) Q factors of various modes, with the phononic bandgap indicated by the gray bar. Adapted from [27].

2.4. Optimization for Q factors

Although many high-Q designs have been found by human intuition, only a handful of studies has looked into using (structural) optimization techniques to improve the dynamic performance of these resonators. Two examples that employ a form of optimization have been listed in this section.

Spider Web Resonators

Inspired by the vibration isolation functionalities of spider web structures found in nature, a parameterized model of a web-like resonator was created. Bayesian optimization was applied to this model, tuning the widths, lengths and quantities of radial and later beams (6 design parameters in total), and using the theory of Dissipation Dilution [22] to estimate the Q factor of a given design. The final structure employs a torsional soft clamping technique, which diminishes the mode curvature close to the clamping sites (in similar fashion to the fractal-shaped resonators by [18, 25]. The optimize mode shape of the resulting structure, as well as a ring-down experiment can be found in Figure 2.3.

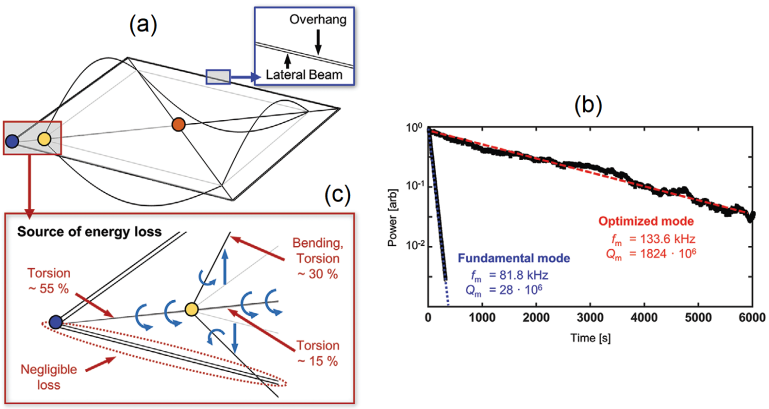

Figure 2.3: (a) Optimized mode of the web-like structure. (b) Ring-down experiment used to characterize the optimized mode. (c) Quantified sources of energy dissipation during vibration. Adapted from [8].

Inversely-Designed Trampoline Structures

Based on the trampoline-shaped resonators used in quantum experiments [6], topology optimization (TO) was used to inversely design trampoline resonators [29, 30] by determining the optimal material distribution within a given domain. In order to model the Q factor of the structure, experimental data was used to create an inverse damping model. Based on two parameters within the model (representing the intrinsic and boundary losses), several designs were found. Three of the resulting designs are displayed in Figure 2.4.

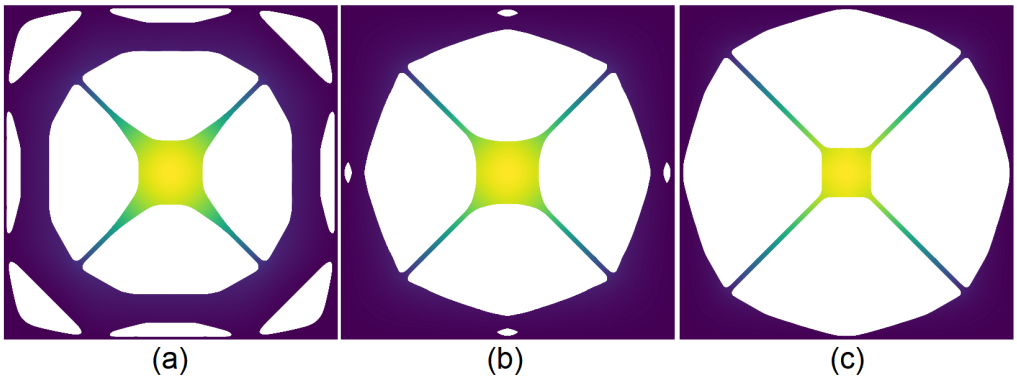

Figure 2.4: Trampoline resonators with their fundamental mode shape, designed with Topology Optimization. Structures (a) and (c) only take a single damping source into account, being intrinsic and boundary losses, respectively. The trampoline in (b) is the outcome when both dissipation mechanisms are equally accounted for in the model. Adapted from [29].

2.5. Conclusion & Research Gap

The structure of nanomechanical resonators is of vital importance to its dynamic properties and performance. This is highlighted by a variety of designs that aim to minimize certain damping mechanisms solely through geometric design. However, only a few studies have looked into using (structural) optimization techniques to design structures with a high Q factor (with two notable examples given in this brief literature review). Although both studies aim to maximize Q (or the $Q \times f$ product), they both depend on *a priori* knowledge input by the user. The first example optimized a parameterized design (with 6 design parameters), which constrained the optimizer to search for structures within the predefined design space. The second example used experimental data to inversely model two sources of damping in combination with TO. As the values of the damping coefficients influenced the (viscous) boundary conditions, the resulting designs were found to strongly depend on their values. Although both studies have resulted in resonator designs with very high Q factors, the *a priori* knowledge involved can be seen as a drawback, as it limits the studies to their specific design cases.

The identified research gap lies in applying optimization techniques to maximize the Q factor of resonators, whilst omitting the need for *a priori* knowledge (either in the form of parameterized design or a damping model based on experimental data). Ideally, filling in this gap results in an optimization methodology that can be used to enhance the Q factor of any geometry, irrespective of its shape or size. Based on this research gap, the following research questions was formulated:

How can topology optimization techniques be applied to optimize the Q factor of nanomechanical resonators, without relying on a priori information?

3

Topology Optimization for Improving Dissipation Dilution in Nanomechanical Resonators

This chapter contains the main work of this thesis, presented in the form of a manuscript. Its format is independent of this thesis (with its own bibliography and appendix), and aims to be eligible for submission to a journal in the field of structural optimization.

Topology Optimization for Improving Dissipation Dilution in Nanomechanical Resonators

H.J. Algra

Abstract

The predominant influence of geometry and tensile stress on the Q factor of nanomechanical resonators is a phenomenon commonly described as dissipation dilution. In recent years, a variety of studies has looked into maximizing this effect, resulting in an assortment of softly-clamped resonator designs. This paper proposes a methodology that uses topology optimization (TO) to design nanomechanical structures with very high Q factors, by maximizing the effects of dissipation dilution. A novel equation, based on the tensile and bending energies of a prestressed finite element model, is proposed to capture this effect. Through adjoint sensitivity analysis, the sensitivity of this function with respect to (changes in) element-level design parameters was determined, which is a capability that is not available in commercial finite element packages. Furthermore, the absence of information required *a priori* to the optimization makes the proposed methodology versatile and easy to use. After verification of the equation and its sensitivity, it is used as an objective in TO to optimize resonator geometries inspired by state-of-the-art resonator designs. Given a thickness of 340nm and prestress of 1GPa, the final designs show a numerical $Q \times f_0$ that competes with optimized designs found in literature.

Keywords: *Nanomechanical resonators, Q factor, topology optimization, adjoint sensitivity analysis*

Introduction

Nanomechanical resonators are ubiquitously present in modern electronics and sensing devices, as they can function as very precise time-keeping oscillators [1] and excellent force [2] and mass [3, 4] sensors. They are also used for a variety of other applications, such as the optomechanical quantum experiments [5, 6]. In all these applications, a limiting factor to their usefulness is the influence of thermal noise, which results in a random force on the oscillating body [7]. This thermal noise force limits the precision with which quantities such as forces, masses, or pressures can be detected [8]. From the fluctuation-dissipation theorem, it is known that the influence of thermal noise increases with resonator mass, temperature, and dissipation rate [7]. Apart from reducing the mass and operation temperature of these oscillators, minimizing the amount of energy they dissipate is a critical aspect when it comes to mitigating the effect of thermal noise [7, 9]. A low dissipation rate has several other benefits that include, but are not limited to, enabling the oscillator to function at low power [9] and a sharper resonance peak, which allows the resonance frequency of the oscillator to be determined more accurately [10].

An important figure of merit commonly used to quantify the performance of resonator designs is known as the Quality factor (Q factor). A higher Q factor coincides with a lower energy dissipation rate, indicating a higher accuracy and usefulness of a sensor. Mathematically this quantity is given as [7]

$$Q = 2\pi \frac{E_s}{\Delta E_d} \ , \tag{1}$$

where E_s represents the total amount of energy stored inside the resonator, and ΔE_d denotes the energy loss per cycle of oscillation. This definition can be best understood by considering a ringdown measurement, where the decaying movement of a freely oscillating resonator is observed. From this definition, it follows that an oscillator's Q factor can be enhanced by either increasing the total energy stored or reducing the energy dissipated per oscillation cycle.

In recent years, resonators portraying increasingly higher Q factors have been designed, using geometric layouts that aim to decrease the effects of specific dissipation mechanisms. A notable example is the use of fractal-shaped resonators [11, 12], which aim to reduce the gradient of the fundamental mode near the clamping points, in order to decrease bending losses. Furthermore, the use of phononic crystals [13–17] has enabled researchers to isolate a higher order vibration mode near the center of a resonating structure, resulting in the reduction of acoustic radiation losses. In every resonator design, the influence of geometry on the Q factor of the mode of interest is evident. The dependency of Q on geometry has encouraged the use of (structural) optimization techniques in the design of high-Q resonators. A

notable example of a resonator that has been designed using optimization is the so-called "spiderweb" resonator [8], which was realized by applying machine learning to optimize a pre-parameterized design. Another study [18] employed topology optimization (TO) to minimize surface and boundary losses, using a damping model based on experimental data.

Notwithstanding the results achieved by these two examples, a drawback to both studies is the knowledge required *a priori*. In case of the "spiderweb" resonators [8], this concerned the parameterization of the structure. This limits the optimization study to geometries that lie within the parameterized design space. Working with TO [18] overcomes this limitation as it is a structural optimization technique that can freely generate structures. However, the study in question used a damping model fit to experimental data to inversely model bending losses and boundary damping. It was found that the optimized resonator designs showed a strong dependency on the damping coefficients, as they influenced the boundary conditions. Furthermore, applying the proposed methodology to problems of different dimensions would most likely require a replication of the fabrication and experimental procedures, which can be costly and time-consuming. To the author's best knowledge, no studies exist that use structural optimization techniques to enhance the dynamic performance of prestressed nanomechanical resonators, without requiring *a priori* user input.

This work aims to fill the identified research gap by defining a novel objective function related to the Q factor of a resonator, which is purely based on a geometry and its static prestressed state. The derivation of this objective can be found under "**Theory**". By applying the adjoint method, the sensitivity of this function with respect to changes in geometry is found, which allows it to be used as an objective in TO. The optimization methodology and sensitivity derivation are described under "**Topology Optimization**" and "**Sensitivity Analysis**", respectively. Numerical results of an optimization study are presented at the end of this work, under "**Simulations**". This work concludes by presenting optimized resonator designs and giving an outlook for future work.

Theory

A. Prestressed finite element analysis

This section describes the fundamentals of prestressed finite element analysis (FEA), which underlies the derivation of the novel objective function as well as the subsequent topology optimization procedure. In order to determine the eigenvalues and modes of a prestressed system, a two-step approach is commonly used [19, 20]. The first step concerns a static analysis, in which the equilibrium displacement and resulting stress distributions are determined. As resonators are generally fabricated from extremely thin membranes, this paper works with T3 shell elements, employing a linearized version of [21]. The assumption is made that a linear analysis suffices for the pre-study. This is valid when the prestress distribution is restricted to in-plane stresses, which is the case here. In FEA, prestress manifests itself as a contribution to the force vector, which is assembled together with the material stiffness matrix at the element level as

$$\boldsymbol{K} = \mathop{\mathbb{A}}_{e} \boldsymbol{D}_{(e)}^{\intercal} \boldsymbol{S}_e \boldsymbol{D}_e \ , \quad \boldsymbol{f}_\sigma = \mathop{\mathbb{A}}_{e} -\boldsymbol{D}_e^{\intercal} \boldsymbol{\sigma}_0 \ , \tag{2}$$

where $\boldsymbol{D}_e$ represents the linear strain-displacement matrix, and $\boldsymbol{S}_e$ is used to denote the constitutive matrix. In this work, the material is considered to be linear and isotropic. This allows the prestress to be expressed as a prestrain through $\boldsymbol{\sigma}_0 = \boldsymbol{S}\boldsymbol{\varepsilon}_0$, where both the prestress $\boldsymbol{\sigma}_0$ and prestrain $\boldsymbol{\varepsilon}_0$ are in Voigt notation. It should be noted that the matrices on the right hand side of both terms in (2) are at the element level. The assembly operation of the element-wise matrices is denoted by $\mathbb{A}$, which results in the global (system) matrices. After boundary conditions are prescribed, the following system can be solved to determine the equilibrium displacements $\boldsymbol{u}_\sigma$

$$\boldsymbol{K}\boldsymbol{u}_\sigma = \boldsymbol{f}_\sigma . \tag{3}$$

Based on the static displacements $\boldsymbol{u}_\sigma$ determined in equation (3), the equilibrium stress level in the elements is computed as:

$$\boldsymbol{\sigma}_{eq}^{(e)} = \boldsymbol{S}_e \boldsymbol{D}_e \boldsymbol{u}_\sigma^{(e)} - \boldsymbol{\sigma}_0 = \boldsymbol{S}_e \left(\boldsymbol{D}_e \boldsymbol{u}_\sigma^{(e)} - \boldsymbol{\varepsilon}_0 \right) . \tag{4}$$

In equation (4) the prestress is expressed as a prestrain using linear elasticity theory, i.e., $\boldsymbol{\sigma}_0 = \boldsymbol{S}\boldsymbol{\varepsilon}_0$. Based on the equilibrium stress state, the geometric stiffness matrix is computed as:

$$\boldsymbol{G} = \mathop{\mathbb{A}}_{e} \boldsymbol{G}_{ij}^{(e)} = \mathop{\mathbb{A}}_{e} \sum_k \sigma_{eq,k}^{(e)} \frac{\partial^2 \varepsilon_k}{\partial u_i \partial u_j} . \tag{5}$$

This matrix is computed by multiplying components of the equilibrium stress vector by a set of coefficients that depend on the geometry, capturing the influence of the stress on the overall stiffness of the system. The following eigenvalue problem is solved to determine the prestressed eigenfrequencies (ω_i^2) and modes ($\boldsymbol{\phi}_i$) of the system.

$$\left(\boldsymbol{K} + \boldsymbol{G} - \omega_i^2 \boldsymbol{M} \right) \boldsymbol{\phi}_i = \boldsymbol{0} \ , \tag{6}$$

where $\boldsymbol{M}$ denotes the mass matrix of the system, which is computed based on the geometry and mass density of the elements.

B. Dissipation Dilution

The aforementioned relation between the geometry, stress state and Q factor can be described by an effect known as "dissipation dilution" [14]. In short, the presence of tensile stress can increase the stored energy in the system without adding loss [22]. In order to model the extent of this enhancement, the following definition for the overall Q factor that a structure exhibits is commonly used:

$$Q = D_Q Q_0 \ , \tag{7}$$

where Q_0 represents the "intrinsic Q factor" of the system, which is limited by intrinsic material damping. This Q_0 corresponds to the Q factor of the structure in an unstressed state, which typically does not exceed $1/\varphi$, with φ denoting the material loss angle (i.e., the delay between stress and strain). The effect of dissipation dilution manifests itself in the factor D_Q, which is multiplied with Q_0 to arrive at the resonator's overall Q factor when tensile stress is applied to the structure. In string resonators, it has been shown that this factor can be approximated as the ratio of tension over bending energy [10]. In this work, this ratio is expressed using the geometric and material stiffness matrices from FEA (pre- and post-multiplied by the mode shape of interest, to arrive at the stored energies). This results in the following definition of D_Q, which defines the objective to be maximized in this study,

$$D_Q \approx \frac{W_t}{W_b} = \frac{\boldsymbol{\phi}^\intercal \boldsymbol{G} \boldsymbol{\phi}}{\boldsymbol{\phi}^\intercal \boldsymbol{K} \boldsymbol{\phi}} \tag{8}$$

This equation relies solely on the matrices and mode shapes described in the aforementioned finite element procedure. This work focuses on optimizing the fundamental (first) eigenmode, which is why the subscript seen in (6) is dropped henceforth. A practical reason for this decision is that the frequency and mode shape of the first eigenmode are easiest to measure. Furthermore, working with higher-order modes in combination with topology optimization adds the additional challenge of mitigating intermediate spurious (low-density) modes.

In literature, a more complicated equation is commonly used to compute D_Q [8, 14], namely

$$D_Q \approx \frac{12(1-\nu^2)}{Eh^2} \frac{\iint \alpha dS}{\iint \beta dS}. \tag{9}$$

In this equation, ν and E indicate the material's Poisson ratio and Young's modulus, respectively. h denotes the thickness of the structure, and the quantities α and β are defined as

$$\begin{aligned} \alpha =& \sigma_{xx} \left(\frac{\partial w}{\partial x}\right)^2 + \sigma_{yy} \left(\frac{\partial w}{\partial y}\right)^2 + 2\sigma_{xy} \frac{\partial w}{\partial x} \frac{\partial w}{\partial y} \ , \\ \beta =& \left(\frac{\partial^2 w}{\partial x^2}\right)^2 + \left(\frac{\partial^2 w}{\partial y^2}\right)^2 + 2\nu \frac{\partial^2 w}{\partial x^2} \frac{\partial^2 w}{\partial y^2} \\ &+ 2\left(1-\nu\right) \frac{\partial^2 w}{\partial x \partial y}. \end{aligned}$$

Here, w represents the out-of-plane displacement of the mode of interest, and the components of $\boldsymbol{\sigma}$ correspond to the equilibrium stress distribution (i.e., from the static analysis). In order to quantitatively compare definitions (8) and (9), both equations were computed for two resonator designs whilst varying a geometric parameter. The resulting dilution factors as a function of these geometric parameters can be found in Figure 1. A strong correspondence can be seen in the plots, which can be attributed to the fact that they are both based on the same theory of dissipation dilution, as explained in [14]. The extended datasets for these results can be found in Appendix A.

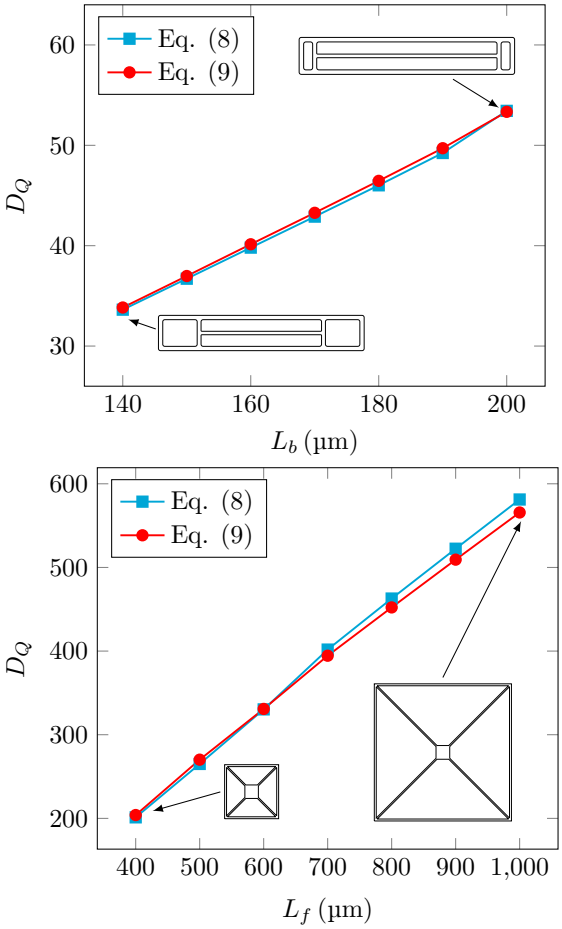

Figure 1: A direct comparison was made between the novel equation for the dilution factor presented in this work (Eq. 8), and a function known from literature (Eq. 9). This was done by numerically computing these equations for two sets of resonators. The first set (top) concerned an H-beam resonator inspired by [9], for which the length of the central beam was varied. The second set (bottom) concerned a trampoline-like structure inspired by [5], for which the length of the outer frame was varied. All designs were evaluated at a thickness of 340nm with a prestress of 1.1GPa, imitating the values used in [9]. The material of choice was Si_3N_4, for which the material properties have been listed in Appendix D.

Topology Optimization

This section explains the fundamentals of the topology optimization (TO) [23] which was the method of choice for this work. In short, TO is a structural optimization technique that seeks the optimal material distribution within a design domain in order to maximize or minimize an objective. This is an iterative process, in which a gradient-

based optimizer gradually adds or removes material in search of an optimal design. For this technique, the optimization algorithm of choice is the method of moving asymptotes (MMA) [24]. A given material distribution is represented on the element-level by a local parameter $\rho_e \in (0, 1]$. For each element, a value of ρ_e close to zero indicates an 'empty' element, and a value close to one indicates a 'filled' element. For numerical stability reasons, a minimum value of ρ is commonly imposed (e.g., $\rho_{min} = 10^{-5}$). In order to determine the structural properties of a design, the Young's modulus is penalized on the element level based on the corresponding design density. After computing the values and gradients of the objective and constraint functions, the MMA algorithm determines an incremental design update to the density in each element. This process is repeated until a convergence criterium is met.

Certain properties such as checkerboarding patterns (i.e., alternating filled and empty elements) may be beneficial to the optimizer, but are nonphysical and impossible to fabricate. To ensure smooth edges and avoid alternating densities, a simple (weighted average) distance filter is applied to the material distribution. This operation results in the local filtered density $\tilde{\rho}_e$, which is found from:

$$\tilde{\rho}_e = \frac{\sum_{i \in N_e} \left(r_f - \|\boldsymbol{x}_e - \boldsymbol{x}_i\|\right) \rho_i}{\sum_{i \in N_e} \left(r_f - \|\boldsymbol{x}_e - \boldsymbol{x}_i\|\right)} \tag{10}$$

For a given element, the set N_e contains all elements of which the centers lie within range of the filter radius r_f. The chosen radius can strongly influence the outcome of the optimization procedure, and is generally used to alleviate mesh-dependency. A downside to using the filtering procedure is the increased presence of regions with intermediate densities (i.e., not close to 0 or 1) within the domain. These do not have a clear physical meaning, and should not be present in the final design. In order to reduce these so-called "gray areas", a projection operation is applied to the filtered densities. The projection used in this work is given below.

$$\bar{\rho}_e = \frac{\tanh \beta\eta + \tanh \beta \left(\tilde{\rho}_e - \eta\right)}{\tanh \beta\eta + \tanh \beta \left(1 - \eta\right)} \tag{11}$$

Here, β and η denote the slope and central point of the projection operation, with typical values being 8 and 0.5, respectively. The projected densities are subsequently related to the Young's modulus of their corresponding element by means of a penalization function. In this study, the Rational Approximation of Material Properties (RAMP) [25] penalization was chosen, as it proved to be effective in a similar TO study [20]. It should be noted that the use of interpolation functions was looked into, such as a modified version of SIMP used in eigenfrequency problems [19, 26, 27]. However, this function was deemed ineffective due to the rise of instabilities in the optimization procedure. The effect of the RAMP function on the local Young's modulus of an element can be expressed as follows [25]:

$$E_e\left(\bar{\rho}_e\right) = E_0 \left[\frac{E_{min}}{E_0} + \frac{\left(1 - \frac{E_{min}}{E_0}\right) \bar{\rho}_e}{1 + q\left(1 - \bar{\rho}_e\right)} \right] \tag{12}$$

Here, E_0 represents the intrinsic Young's modulus of the material, and E_{min} indicates the minimum of E within the domain. The ratio of E_{min}/E_0 denotes the minimum ratio of Young's moduli between high-density and low-density elements (irrespective of the minimum design density ρ_{min}). In this study, 10^{-6} was chosen. Controlling this ratio also helps to prevent the appearance of spurious modes, which are eigenmodes present in the low-density (void) regions of the domain. These are caused by a high local mass-to-stiffness ratio, and can be problematic to the optimization procedure when not accounted for. In equation (12), the terms between the square brackets represent the penalization that is multiplied with each element's local stiffness matrix (which scales with E_0).

In order to capture the effect of an element's density on its local mass, a linear interpolation was used. This function is given as:

$$M_e(\bar{\rho}) = M_0 \left[\left(1 - \frac{M_{min}}{M_0}\right) \bar{\rho}_e + \frac{M_{min}}{M_0} \right] \tag{13}$$

The ratio of M_{min}/M_0 indicates the minimum mass ratio between void and filled elements, which was set to 10^{-7} in this work.

In order to prevent instabilities in low-density elements, an interpolation similar to the projection in equation (11) can be applied to the static displacement when computing the stresses with (4). This interpolation can be expressed and applied as follows [28]:

$$\begin{aligned} \alpha_e(E_e) &= \frac{\tanh \gamma\nu + \tanh \gamma \left(E_e/E_0 - \nu\right)}{\tanh \gamma\nu + \tanh \gamma \left(1 - \nu\right)} \\ \tilde{\boldsymbol{u}}_\sigma^{(e)} &= \alpha_e \boldsymbol{u}_\sigma^{(e)} \\ \boldsymbol{\sigma}_{eq}^{(e)} &= \boldsymbol{S}_e \left(\boldsymbol{D}_e \tilde{\boldsymbol{u}}_\sigma^{(e)} - \boldsymbol{\varepsilon}_0\right) \end{aligned} \tag{14}$$

For every element, the parameter α_e is calculated, which depends on the ratio of the element Young's modulus over the material's Young's modulus. This value is then used to determine the interpolated displacement, denoted as $\tilde{\boldsymbol{u}}_\sigma^{(e)}$. For elements with a low Young's modulus, this operation reduces the effect of static displacement in the the computation of the element-level stresses, $\boldsymbol{\sigma}^{(e)}$. The projection is controlled by the parameters γ and ν, represent the slope and mid-point, similar to β and η in equation (11). Typical values for these parameters are $\gamma = 30$ and $\nu = 0.05$. As this projection influences the computation of element-level stresses, it also has an effect on the relation between the geometric stiffness matrix (5) and the design variables ρ_e. This is included in the sensitivity analysis of the matrix $\boldsymbol{G}$, which is discussed in Appendix B.1.

Sensitivity Analysis

In order to determine the sensitivity of the objective function (eq. 8) with respect to a design density ρ_e, the adjoint method was used. This involves augmenting the objective is with the constitutive equations as constraints, using Lagrange multipliers. By choosing specific values for the Lagrange multipliers computationally expensive terms such as $\frac{d\boldsymbol{u}_\sigma}{d\rho_e}$ and $\frac{d\boldsymbol{\phi}}{d\rho_e}$ can be eliminated from the sensitivity expression. The augmented expression reads:

$$\begin{aligned} L = &\frac{\boldsymbol{\phi}^\intercal \boldsymbol{G} \boldsymbol{\phi}}{\boldsymbol{\phi}^\intercal \boldsymbol{K} \boldsymbol{\phi}} + \boldsymbol{\lambda}_1^\intercal \left(\boldsymbol{f}_\sigma - \boldsymbol{K}\boldsymbol{u}_\sigma\right) \\ &+ \boldsymbol{\lambda}_2^\intercal \left(\boldsymbol{K} + \boldsymbol{G} - \omega^2 \boldsymbol{M}\right) \boldsymbol{\phi} + \lambda_3 \left(\boldsymbol{\phi}^\intercal \boldsymbol{M} \boldsymbol{\phi} - 1\right) \end{aligned} \tag{15}$$

Differentiating this function with respect to a design variable ρ_e results in the following expression:

$$\begin{aligned} \frac{dL}{d\rho} = &\frac{\boldsymbol{\phi}^\intercal \frac{\partial \boldsymbol{G}}{\partial \rho} \boldsymbol{\phi}}{\boldsymbol{\phi}^\intercal \boldsymbol{K} \boldsymbol{\phi}} - \frac{\boldsymbol{\phi}^\intercal \boldsymbol{G} \boldsymbol{\phi} \cdot \boldsymbol{\phi}^\intercal \frac{d\boldsymbol{K}}{d\rho} \boldsymbol{\phi}}{\left(\boldsymbol{\phi}^\intercal \boldsymbol{K} \boldsymbol{\phi}\right)^2} \\ &+ \boldsymbol{\lambda}_1^\intercal \left(\frac{d\boldsymbol{f}_\sigma}{d\rho} - \frac{d\boldsymbol{K}}{d\rho} \boldsymbol{u}_\sigma\right) \\ &+ \boldsymbol{\lambda}_2^\intercal \left(\frac{d\boldsymbol{K}}{d\rho} + \frac{\partial \boldsymbol{G}}{\partial \rho} - \omega^2 \frac{d\boldsymbol{M}}{d\rho}\right) \boldsymbol{\phi} \end{aligned} \tag{16}$$

In these equations the subscript in ρ_e is omitted for clarity. The system matrices and force vector are related to the design variables through the filtering (10), projection (11) and penalization (12 & 13) equations mentioned in this section. The complete sensitivity analysis, (including expressions for the Lagrange multipliers), can be found in Appendix B.3.

The accuracy of the analytical sensitivity (16) was verified by means of the finite difference (FD) check, using a central difference scheme for the first order derivative. The relative difference between the analytical and FD sensitivities has been plotted in Figure 2, converging at a FD step size of approximately 2×10^{-4}. This step size was found to correspond to a mean absolute relative difference of 8×10^{-9}.

Simulations

In this section the results of using topology optimization (TO) to maximize Eq. (8) are presented. The trampoline structure by [5] was used as a reference, as a previous study [18] has also looked into optimizing the Q factors of these trampolines using TO. An important distinction between this work and previous works is that a thickness of 340nm (akin to [9]) was used to ensure stability in the optimization procedure. The measurements in [5] and [18] used 50nm, but optimizations using this thickness resulted in compressive instabilities (indicated by negative values in the tangent stiffness matrix).

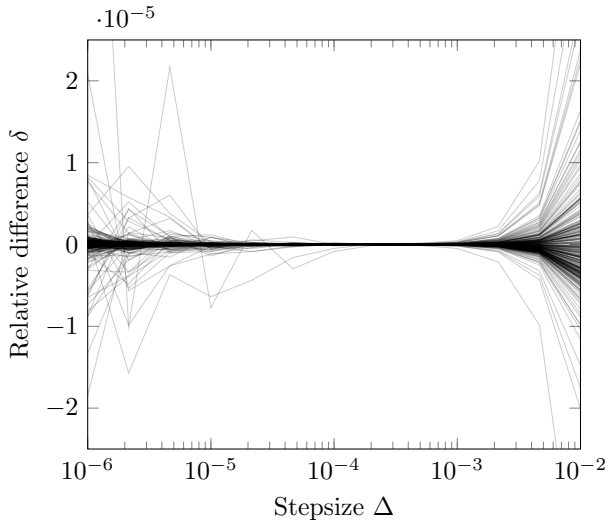

Figure 2: The analytical expression for the sensitivity (eq. 16) was verified using a finite difference (FD) approach. This was done by plotting the relative difference between (eq. 16) and the FD sensitivity as a function of the FD step size. Further details on the FD verification can be found in Appendix C.

The optimization procedure was carried out using prestressed T3 shell elements, using a linearized version of the formulation presented in [21]. The aforementioned filtering (10), projection (11) and penalization (12 & 13) functions were used to relate the design densities to element-level material properties. A constant filter radius of 3 elements was chosen, in combination with a projection slope that started at 1. This slope was gradually increased to 64 to slowly reduce the presence of intermediate elements inside the domain. Furthermore, a lower bound of 400kHz was imposed on the first eigenfrequency of the problem. Numerical tests in this work and the work of others [20] indicates that fragile or nearly-disconnected structures can portray an extremely high Q factor. Because such a system is not manufacturable or even physical, this constraint was added to ensure a minimum level of "connectedness" to the boundaries of the system. Furthermore, a volumetric fraction limit of 0.5 was imposed on all designs, in order to use the same amount of material as [18]. This upper bound on the material present in the design ensures that the effects of dissipation dilution are dominant in the structure. A resonator design that is nearly "filled-in" with mass can have a theoretical Q that is very high (and a very low frequency) purely based on dissipation dilution, but will most show likely a discrepancy between theoretical and experimental results as other effects such acoustic losses can dictate its dynamic performance.

A qualitative observation was made that the values of the frequency lower bound and volumetric fraction limits should be chosen carefully. If a structure's frequency lower bound is too low, then it can become disconnected

and infeasible as previously mentioned. Conversely, if the frequency lower bound is too high, the optimizer seeks to satisfy the frequency constraint and the optimization procedure does not result in an increased D_Q factor. A supporting illustration of the latter case has been included in Appendix E, where the resulting geometry showed a strong correspondence to the result of a prestressed frequency maximization study [19].

The non convexity of the problem at hand was highlighted by the dependency of the final results on the initial material distribution. Two different designs were obtained when starting with a homogeneous density distribution versus a trampoline-like structure. These procedures are summarized in Figures 3 and 4. The final designs were evaluated at a projection slope of 300 to verify whether they depend on intermediate densities. As no significant change was detected in the consequently computed objective function, the designs were found not to rely on intermediate density values.

A more robust way of ensuring that the final design does not rely on intermediate densities is by employing the "robust formulation" [28]. However, the main drawback of this formulation is the associated increase in computation time. For this reason, it was not used in the final results of this study. A comparative simulation was carried out with identical optimization settings, which resulted in a very similar design. For future work, working with this methodology (summarized in Appendix F) is recommended as the frequency lower bound can be decreased whilst ensuring connectedness to the surrounding support structure.

A comparison was made between the geometries obtained with the optimization procedure described in this work, and two existing resonator designs. The first of these was also found using TO [18], where the bending losses of a damping model based on experimental data were minimized. The second design was used by [5] to conduct quantum experiments. In their respective works, these two state-of-the-art resonators worked with a membrane thickness of 50nm. As previously mentioned, the optimization procedure in this work was found to be unstable at this thickness due to negative stiffness values in low density elements (caused by compression). In order to study the effect of a different thickness on the geometries produced in this work, the performance of the newly found designs as well as the reference designs was evaluated at both 120nm and 340nm (for a prestress value of 1GPa). The final comparison used COMSOL, which is a commercial finite element package, to load the final black-and-white geometries using the built-in image-to-curve feature (threshold of 0.5). Furthermore, the approximation $Q_0 \approx 6900 \times h/100$[nm] was used [8] (where h denotes the thickness) to compute the intrinsic Q factor (i.e., the Q factor of the unstressed state).

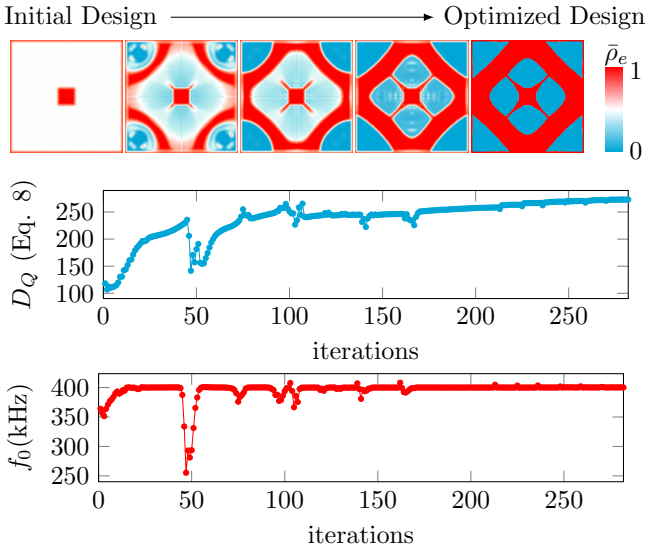

Figure 3: TO procedure for a resonator of 340nm thickness with a prestress of 1GPa. A volumetric fraction of 0.5 and frequency lower bound of 400kHz were imposed. The overall geometry is 700×700µm, with a 100×100µm fixed region at the center, and a fixed outside frame of 5µm. Starting with a homogeneous material distribution results in a final $D_Q \approx 275$. The material of choice was Si_3N_4, for which the material properties have been listed in Appendix D.

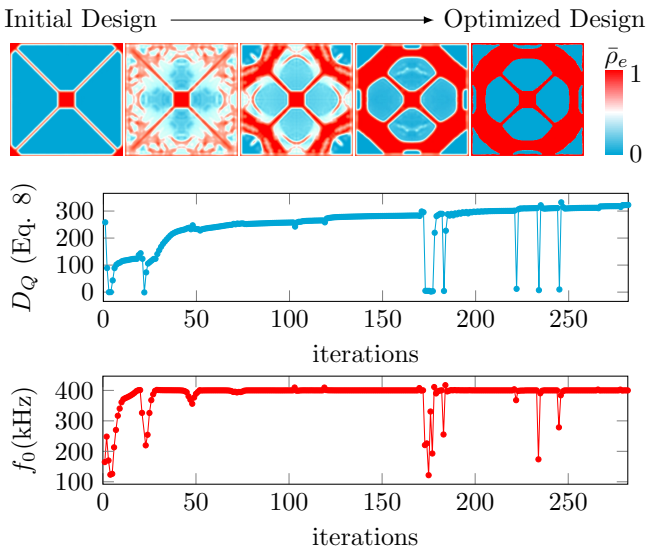

Figure 4: TO procedure for a resonator of 340nm thickness with a prestress of 1GPa. A volumetric fraction of 0.5 and frequency lower bound of 400kHz were imposed. The overall geometry is 700×700 µm, with a 100×100 µm fixed region at the center, and a fixed outside frame of 5 µm. Starting with a trampoline structure results in a final $D_Q \approx 330$. The material of choice was Si_3N_4, for which the material properties have been listed in Appendix D.

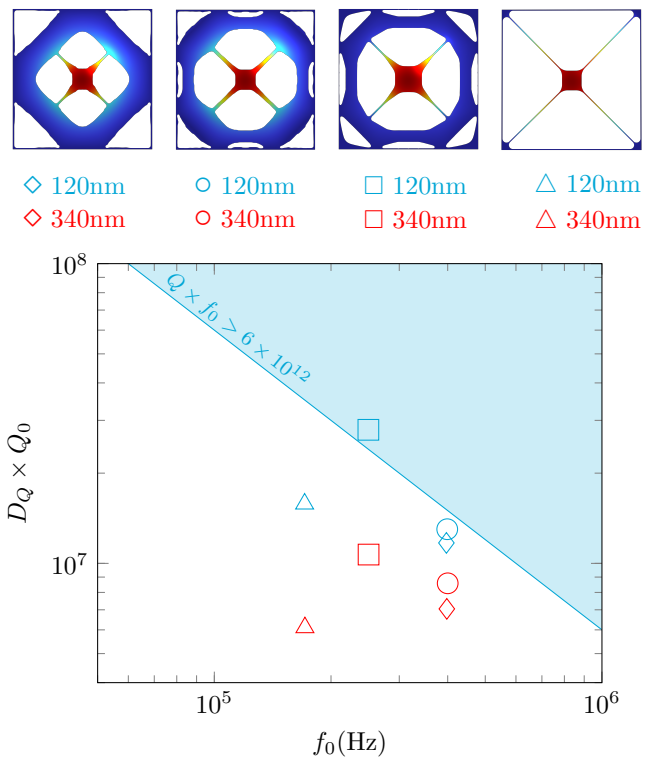

Figure 5: Comparison of $Q \times f_0$ performance of four resonator designs. The two leftmost resonator geometries were designed in this work, followed by an optimized design from [18] and the original trampoline-like structure by [5]. All geometries are 700 × 700µm, with a central 100 × 100µm pad at the center. Dilution factors were computed in COMSOL using equation 9, and the fundamental Q_0 was computed using $Q_0 \approx 6900 \times h/100$[nm], with h being the thickness [8].

Due to the well-known trade-off between a high dilution factor and fundamental frequency, the $Q \times f_0$ product was used as a figure of merit in this comparison. An overview of this comparison can be found in Figure 5, where the region of $Q \times f_0 > 6 \times 10^{12}$ indicates the lower bound required for coherent quantum experiments [5, 18]. For actual quantum experiments, a higher prestress and lower thickness can be used, which should lead to higher dilution factors and higher $Q \times f_0$ products. Furthermore, the computed Q factors rely solely on the effects of dissipation dilution and neglect damping sources such as acoustic radiation. The final results show that the designs obtained in this study (displayed as diamonds and squares in Figure 5) have a lower dilution factor compared to the optimized results by [18], but a higher fundamental frequency, which results in a very comparable $Q \times f_0$ product.

Discussion

In nanomechanical resonators, the geometry and static stress distribution primarily affect the Q factor through an effect called dissipation dilution. This work demonstrates that this effect can accurately be modelled using a novel equation based on the mode shapes and system matrices of a prestressed finite element model. Through adjoint analysis, the analytical gradient of this equation with respect to element-level design parameters was determined, which allowed it to be used as an objective for topology optimization (TO). By using the newly found expression in combination with TO, resonator designs were found with enhanced Q factors and $Q \times f_0$ products comparable to results found in literature [18].

The key advantage of the methodology employed in this work is that no *a priori* knowledge is required as user input to the optimization procedure. Previous works aimed at enhancing the Q factor relied on user input in various forms, such as a simplified design space or results from experiments. By omitting *a priori* knowledge the methodology can directly be applied in design cases (no new experimental data or re-parameterization is required). In order to compare the performance of this work to methods found in literature, the problem of maximizing the Q factor of a trampoline setup [5] was looked into. This setup was chosen due to the availability of previous work [18] which looked into the same problem. The final resonator designs found in this work portray $Q \times f_0$ products which are very comparable to those found in literature, which indicates that the proposed methodology performs well compared to other approaches.

It is highlighted that the simulation results displayed at the end of this work are exploratory in nature. Conducting a numerical study that contains more extensive simulations is appropriate, as certain aspects of the optimization procedure were only briefly looked into. Important aspects include working with a finer mesh to allow designs to have smaller features, applying the robust methodology (summarized in Appendix F) and investigating outcomes that use different starting configurations. The latter has shown to be an important factor in the optimization procedure, as the simulations results were shown to be dependent on the initial material distribution. Furthermore, applying this work's methodology to design resonators of different dimensions (e.g., H-beams as studied in [9]) is a diverse and interesting avenue for future work.

Finally, experimental results (e.g., in the form of ringdown experiments) are indispensable when it comes to the verification of numerical results. An aspect which can be investigated further and would contribute to the possibility of experiments are the addition of manufacturing constraints. In this work, a frequency lower bound was added to ensure connectedness to the boundaries of the system. However, other features such as a limit to the maximum stress, or a constraint on the minimum and/or maximum feature size could be investigated to ensure that designs are suitable for fabrication.

References

[1] T. Nguyuen. "MEMS technology for timing and frequency control". In: *IEEE Transactions on Ultrasonics, Ferroelectrics, and Frequency Control* 54.2 (2007), pp. 251–270. DOI: 10.1109/TUFFC.2007.240.

[2] H.J. Mamin and D. Rugar. "Sub-attonewton force detection at millikelvin temperatures". In: *Applies Physics Letters* 79.3358 (2001). DOI: 10.1063/1.141825.

[3] J. Chaste, A. Eichler, J. Moser, G. Ceballos, R. Rurali, and A. Bachtold. "A nanomechanical mass sensor with yoctogram resolution". In: *Nature Nanotechnology* 7 (2012), pp. 301–304. DOI: 10.1038/NNANO.2012.42.

[4] Thomas Burg, Michel Godin, Scott Knudsen, Wenjiang Shen, Greg Carlson, John Foster, Ken Babock, and Scott Manalis. "Weighing of biomolecules, single cells and single nanoparticles in fluid". In: *Nature* 446 (2007), pp. 1066–1069. DOI: 10.1038/nature05741.

[5] R. Norte, J. Moura, and S. Gröblacher. "Mechanical Resonators for Quantum Optomechanics Experiments at Room Temperature". In: *Phyical Review Letters* 116.147202 (2016). DOI: 10.1103/PhysRevLett.116.147202.

[6] A. O'Connell, M. Hofheinz, M. Ansmann, R. Bialczak, M. Leander, E. Lucero, M. Neeley, D. Sank, H. Wang, M. Weides, J. Wenner, J. Martinis, and A. Cleland. "Quantum ground state and single-phonon control of a mechanical resonator". In: *Nature* 464 (2010), pp. 697–703. DOI: 10.1038/nature08967.

[7] S. Fedorov. "Mechanical resonators with high dissipation dilution in precision and quantum measurements". PhD thesis. École Polytechnique Fédérale de Lausanne, Jan. 2021.

[8] D. Shin, A. Cupertino, M. De Jong, P. Steeneken, and M. Bessa. "Spiderweb Nanomechanical Resonators via Bayesian Optimization: Inspired by Nature and Guided by Machine Learning". In: *Advanced Materials* 34.3 (2021). DOI: 10.1002/adma.202106248.

[9] Z. Li, M. Xu, R. Norte, F. Alijani, A. Aragón, F. van Keulen, and P. Steeneken. "Tuning the Q-factor of Nanomechanical String Resonators by Torsion Support Design". In: *Applied Physics Letters* 122.1 (2023). DOI: 10.1063/5.0133177.

[10] S. Schmid, K. D. Jensen, K. H. Nielsen, and A. Boisen. "Damping mechanisms in high-Q micro and nanomechanical string resonators". In: *Phys. Rev. B* 84 (16 2011), p. 165307. DOI: 10.1103/PhysRevB.84.165307.

[11] S. Fedorov, A. Beccari, N. Engelsen, and T. Kippenberg. "Fractal-like Mechanical Resonators with a Soft-Clamped Fundamental Mode". In: *Physical Review letters* 124.025502 (2020). DOI: 10.1103/PhysRevLett.124.025502.

[12] A. Beccari, M. Beryehi, R. Groth, S. Fedorov, A. Arabmohegi, T. Kippenberg, and N. Engelsen. "Hierarchical tensile structures with ultralow mechanical dissipation". In: *Nature Communications* 13.3097 (2021). DOI: 10.1038/s41467-022-30586-z.

[13] Y. Tsaturyan, A. Barg, E. Polzik, and A. Schliesser. "Ultracoherent nanomechanical resonators via soft clamping and dissipation dilution". In: *Nature Nanotechnology* 12 (2017), pp. 776–784. DOI: 10.1038/NNANO.2017.101.

[14] S. Fedorov, N. Engelsen, A. Ghadimi, M. Bereyhi, R. Schilling, D. Wilson, and T. Kippenberg. "Generalized dissipation dilution in strained mechanical resonators". In: *Physical Review Letters* 99.054107 (2019). DOI: 10.1103/PhysRevB.99.054107.

[15] A. Beccari, D. Visani, S. Fedorov, M. Beryehi, V. Boureau, N. Engelsen, and T. Kippenberg. "Strained crystalline nanomechanical resonators with quality factors above 10 billion". In: *Nature Physics* 18 (2022), pp. 436–441. DOI: 10.1038/s41567-021-01498-4.

[16] A. H. Ghadimi, D. Wilson, and T. Kippenberg. "Radiation and Internal Loss Engineering of High-Stress Silicon Nitride Nanobeams". In: *Nano Letters* 17 (2017), pp. 3501–3505. DOI: 10.1021/acs.nanolett.7b00573.

[17] T. Gisler, M. Helal, D. Sabonis, U. Grob, M. Hénritier, C. Degen, A. Ghadimi, and A. Eichler. "Soft-Clamped Silicon Nitride String Resonators at Millikelvin Temperatures". In: *Physical Review Letters* 129.104301 (2022). DOI: 10.1103/PhysRevLett.129.104301.

[18] D. Høj, F. Wang, W. Gao, U. Hoff, O. Sigmund, and U. Andersen. "Ultra-coherent nanomechanical resonators based on inverse design". In: *Nature Communications* 12.5766 (2021). DOI: 10.1038/s41467-021-26102-4.

[19] N.L. Pedersen. "On topology optimization of plates with prestress". In: *International Journal for Numerical Methods in Engineering* 51 (2001), pp. 225–239. DOI: 10.1002/nme.162.

[20] W. Gao, F. Wang, and O. Sigmund. "Systematic design of high-Q prestressed micro membrane resonators". In: *Computer Methods in Applied Mechanics and Engineerig* 361.112692 (2020). DOI: 10.1016/j.cma.2019.112692.

[21] F. Van Keulen. "A geometrically nonlinear curved shell element with constant stress resultants". In: *Computer Methods in Applied Mechanics and Engineering* 106.3 (1993), pp. 315–352. DOI: 10.1016/0045-7825(93)90093-D.

[22] J.R. Pratt, A. Agrawal, C. Condos, C. Pluchar, S. Sclamminger, and D. Wilson. "Nanoscale Torsional Dissipation Dilution for Quantum Experiments and Precision Measurement". In: *American Physical Society* 13.011018 (2023). DOI: 10.1103/PhysRevX.13.011018.

[23] M.P. Bendsøe and O. Sigmund. *Topology Optimization Theory, Methods and Applications*. 1st ed. Springer, 2004. DOI: 10.1007/978-3-662-05086-6.

[24] K. Svanberg. "The Method of Moving Asymptotes - A New Method for Structural Optimization". In: *International Journal for Numerical Methods in Engineering* 24 (1987), pp. 359–373. DOI: 10.1002/nme.1620240207.

[25] K. Svanberg M. Stolpe. "An alternative interpolation scheme for minimum compliance topology optimization". In: *Structural and Multidisciplinary Optimization* 22 (2001), pp. 116–124. DOI: 10.1007/s001580100129.

[26] N.L. Pedersen. "Maximization of eigenvalues using topology optimization". In: *Structural Multidisciplinary Optimization* 20 (2000), pp. 2–11. DOI: 10.1007/s001580050130.

[27] A. Delissen, E. Boots, D. Laro, H. Kleijnen, F. Van Keulen, and M. Langelaar. "Realization and assessment of metal additive manufacturing and topology optimization for high-precision motion systems". In: *Additive Manufacturing* 58.103012 (2022). DOI: 10.1016/j.addma.2022.103012.

[28] F. Wang, B. Lazarov, O. Sigmund, and J. Jensen. "Interpolation scheme for fictitious domain techniques and topology optimization of finite strain elastic problems". In: *Computer Methods in Applied Mechanics and Engineering* 276 (2014), pp. 453–472. DOI: 10.1016/j.cma.2014.03.021.

[29] T. Tsai and C. Cheng. "Structural design for desired eigenfrequencies and mode shapes using topology optimization". In: *Structural Multidisciplinary Optimization* 27 (2013), pp. 673–686. DOI: 10.1007/s00158-012-0840-2.

[30] J.T. Oden C.A. Duarte I. Babuška. "Generalized finite element methods for three-dimensional structural mechanics problems". In: *Computers & Structures* 77.2 (2000), pp. 215–232. DOI: 10.1016/S0045-7949(99)00211-4.

[31] Alejandro M. Aragón and C. Armando Duarte. *Fundamentals of Enriched Finite Element Methods*. 1st ed. ISBN: 9780323855150. Elsevier, 2023.

Appendices

A Dataset for D_Q comparison

	`Hybrida` (In-house FEA)			COMSOL (Commercial)		
L_b [µm]	D_Q from (8)	$\texttt{max}(\boldsymbol{u}_\sigma)$ [mm]	f_0 [kHz]	D_Q from (9)	$\texttt{max}(\boldsymbol{u}_\sigma)$ [mm]	f_0 [kHz]
140	3.3624E+01	1.4373E-04	1.2531E+03	3.3841E+01	1.4447E-04	1.2517E+03
150	3.6710E+01	1.4849E-04	1.1900E+03	3.6978E+01	1.4925E-04	1.1888E+03
160	3.9806E+01	1.5286E-04	1.1336E+03	4.0142E+01	1.5374E-04	1.1324E+03
170	4.2895E+01	1.5708E-04	1.0826E+03	4.3275E+01	1.5797E-04	1.0815E+03
180	4.6015E+01	1.6102E-04	1.0364E+03	4.6459E+01	1.6193E-04	1.0354E+03
190	4.9235E+01	1.6456E-04	9.9440E+02	4.9711E+01	1.6560E-04	9.9347E+02
200	5.3433E+01	1.6460E-04	9.6607E+02	5.3338E+01	1.6886E-04	9.5558E+02

Table 1: Numerical comparison data for the H-beam resonators

	`Hybrida` (In-house FEA)			COMSOL (Commercial)		
L_s [µm]	D_Q from (8)	$\texttt{max}(\boldsymbol{u}_\sigma)$ [mm]	f_0 [kHz]	D_Q from (9)	$\texttt{max}(\boldsymbol{u}_\sigma)$ [mm]	f_0 [kHz]
400	2.0122E+02	1.6419E-04	3.5974E+02	2.0398E+02	1.6418E-04	3.5901E+02
500	2.6507E+02	1.6438E-04	2.9352E+02	2.7018E+02	1.6442E-04	2.9297E+02
600	3.3029E+02	1.6451E-04	2.4958E+02	3.3083E+02	1.6458E-04	2.4911E+02
700	4.0178E+02	1.6464E-04	2.1789E+02	3.9445E+02	1.6468E-04	2.1746E+02
800	4.6280E+02	1.6471E-04	1.9366E+02	4.5220E+02	1.6476E-04	1.9334E+02
900	5.2237E+02	1.6476E-04	1.7451E+02	5.0931E+02	1.6481E-04	1.7426E+02
1000	5.8122E+02	1.6481E-04	1.5894E+02	5.6570E+02	1.6486E-04	1.5874E+02

Table 2: Numerical comparison data for the trampoline resonators

B Sensitivity Analysis

This section extensively describes the sensitivity analysis involved in this work. It starts by summarizing the sensitivity of the geometric stiffness matrix, followed by the sensitivities of prestressed eigenvalue problems. An understanding of these concepts is beneficial to understanding (and implementing) the sensitivity of the novel dilution factor equation. In this chapter, the subscript from ρ_e is omitted for clarity.

B.1 Geometric Stiffness Matrix Derivatives

Computing the sensitivity of the $\boldsymbol{G}$ matrix with respect to a design density is not straightforward, as it has an explicit and implicit dependence on ρ. The explicit dependence is a result of its direct dependence on each element's penalized Young's modulus, (which linearly scales the elasticity matrix $\boldsymbol{S}$). Its implicit dependence stems from the dependence of $\boldsymbol{G}$ on $\boldsymbol{u}_\sigma(\rho)$. To incorporate both dependencies, the chain rule is applied in the computation of $\frac{d\boldsymbol{G}}{d\rho}$. This is done as follows:

$$\frac{d\boldsymbol{G}}{d\rho} = \frac{\partial \boldsymbol{G}}{\partial \rho} + \frac{\partial \boldsymbol{G}}{\partial \boldsymbol{u}_\sigma}\frac{d\boldsymbol{u}_\sigma}{d\rho} \tag{17}$$

The partial derivative of $\boldsymbol{G}$ with respect to ρ in (17) can be computed in a straightforward manner, as it concerns differentiating the penalization function of each element. Taking the derivative of $\boldsymbol{G}$ with respect to $\boldsymbol{u}_\sigma$ is slightly more complicated, as it will result in a three-dimensional tensor for each element. The definition for this tensor is given in index notation below.

$$\frac{\partial \boldsymbol{G}}{\partial \boldsymbol{u}_\sigma} = \frac{\partial \boldsymbol{G}}{\partial \boldsymbol{\sigma}}\frac{\partial \boldsymbol{\sigma}}{\partial \boldsymbol{u}_\sigma} \;\Rightarrow\; \frac{\partial G_{ij}}{\partial u_\alpha} = \frac{\partial G_{ij}}{\partial \sigma_k}\frac{\partial \sigma_k}{\partial u_\alpha} = \frac{\partial^2 \varepsilon_k}{\partial u_i \partial u_j}\left[\boldsymbol{SD}\right]_{k\alpha} \tag{18}$$

In the FEA model used, the terms computed in (18) were stored in a four-dimensional tensor, contained in the variable `dGdu`. In the ordering convention used, tensory entry `dGdu[e,i,j,a]` contained $G_{ij}^{(e)}$ differentiated with respect to displacement component `a`.

If the static displacements are penalized (i.e., to prevent wrinkling instabilities as mentioned by [20]), the displacement penalization must be taken into account when computing (17). If the penalized displacement is found from $\tilde{\boldsymbol{u}}_\sigma^{(e)} = \alpha_e \boldsymbol{u}_\sigma^{(e)}$, then the derivative of $\boldsymbol{G}$ with respect to the design density becomes:

$$\frac{d\boldsymbol{G}}{d\rho} = \frac{\partial \boldsymbol{G}}{\partial \rho} + \frac{\partial \boldsymbol{G}}{\partial \tilde{\boldsymbol{u}}} \left(\boldsymbol{u}_\sigma \circ \frac{d\boldsymbol{\alpha}}{d\rho} + \boldsymbol{\alpha} \circ \frac{d\tilde{\boldsymbol{u}}_\sigma}{d\rho} \right) \tag{19}$$

Here $\circ$ represents the Hadamard product (indicating element-wise multiplication). As $\boldsymbol{\alpha}$ only depends on the element of interest, the second right-hand-side term will be zero for all elements, except for the element for which $\frac{d\boldsymbol{G}}{d\rho}$ is computed.

B.2 Sensitivity Analysis of Eigenfrequencies

In this subsection the sensitivity analysis of prestressed eigenfrequencies as presented for plates by [19] is briefly summarized. The eigenvalue problem of a prestressed system is augmented with the static equilibrium equation of the system using a Lagrange multiplier denoted as $\boldsymbol{\mu}$. This results in the following expression:

$$\boldsymbol{\phi}^\intercal \left(\boldsymbol{K} + \boldsymbol{G} - \omega^2 \boldsymbol{M} \right) \boldsymbol{\phi} + \boldsymbol{\mu}^T \left(\boldsymbol{f}_\sigma - \boldsymbol{K} \boldsymbol{u}_\sigma \right) = 0 \tag{20}$$

Differentiating (20) with respect to a design variable ρ, and assuming mass-normalized modes results in the following definition for the eigenfrequency sensitivity:

$$\frac{d\omega^2}{d\rho} = \boldsymbol{\phi}^\intercal \left(\frac{d\boldsymbol{K}}{d\rho} + \frac{\partial \boldsymbol{G}}{\partial \rho} - \omega^2 \frac{d\boldsymbol{M}}{d\rho} \right) \boldsymbol{\phi} + \boldsymbol{\mu}^\intercal \left(\frac{d\boldsymbol{f}_\sigma}{d\rho} - \frac{d\boldsymbol{K}}{d\rho} \boldsymbol{u}_\sigma \right) \tag{21}$$

In order for this definition to hold, the following problem must be solved for the Lagrange multiplier $\boldsymbol{\mu}$:

$$\boldsymbol{K} \boldsymbol{\mu} = \boldsymbol{\phi}^\intercal \frac{\partial \boldsymbol{G}}{\partial \boldsymbol{u}_\sigma} \boldsymbol{\phi} \tag{22}$$

B.3 Sensitivity Analysis of the D_Q Objective

The objective function (8) is augmented with the null-form of three constitutive relations using by Lagrange multipliers. These multipliers have been denoted as $\boldsymbol{\lambda}_1$, $\boldsymbol{\lambda}_2$ and λ_3 in the equation below.

$$L = \frac{\boldsymbol{\phi}^\intercal \boldsymbol{G} \boldsymbol{\phi}}{\boldsymbol{\phi}^\intercal \boldsymbol{K} \boldsymbol{\phi}} + \boldsymbol{\lambda}_1^\intercal \left(\boldsymbol{f}_\sigma - \boldsymbol{K} \boldsymbol{u}_\sigma \right) + \boldsymbol{\lambda}_2^\intercal \left(\boldsymbol{K} + \boldsymbol{G} - \omega^2 \boldsymbol{M} \right) \boldsymbol{\phi} + \lambda_3 \left(\boldsymbol{\phi}^\intercal \boldsymbol{M} \boldsymbol{\phi} - 1 \right) \tag{23}$$

Taking the derivative of this function with respect to the design density results and inserting 17 results in:

$$\begin{aligned} \frac{dL}{d\rho} = & \frac{\boldsymbol{\phi}^\intercal \frac{\partial \boldsymbol{G}}{\partial \rho} \boldsymbol{\phi}}{\boldsymbol{\phi}^\intercal \boldsymbol{K} \boldsymbol{\phi}} - \frac{\boldsymbol{\phi}^\intercal \boldsymbol{G} \boldsymbol{\phi} \cdot \boldsymbol{\phi}^\intercal \frac{d\boldsymbol{K}}{d\rho} \boldsymbol{\phi}}{\left(\boldsymbol{\phi}^\intercal \boldsymbol{K} \boldsymbol{\phi} \right)^2} + \boldsymbol{\lambda}_1^\intercal \left(\frac{d\boldsymbol{f}_\sigma}{d\rho} - \frac{d\boldsymbol{K}}{d\rho} \boldsymbol{u}_\sigma \right) \\ & + \boldsymbol{\lambda}_2^\intercal \left(\frac{d\boldsymbol{K}}{d\rho} + \frac{\partial \boldsymbol{G}}{\partial \rho} - \frac{d\omega^2}{d\rho} \boldsymbol{M} - \omega^2 \frac{d\boldsymbol{M}}{d\rho} \right) \boldsymbol{\phi} + \lambda_3 \left(\boldsymbol{\phi}^T \frac{d\boldsymbol{M}}{d\rho} \boldsymbol{\phi} \right) \\ & + \left[\frac{2\boldsymbol{\phi}^\intercal \boldsymbol{G}}{\boldsymbol{\phi}^\intercal \boldsymbol{K} \boldsymbol{\phi}} - \frac{\boldsymbol{\phi}^\intercal \boldsymbol{G} \boldsymbol{\phi} \cdot 2\boldsymbol{\phi}^\intercal \boldsymbol{K}}{\left(\boldsymbol{\phi}^\intercal \boldsymbol{K} \boldsymbol{\phi} \right)^2} + \boldsymbol{\lambda}_2^\intercal \left(\boldsymbol{K} + \boldsymbol{G} - \omega^2 \boldsymbol{M} \right) + \lambda_3 \cdot 2\boldsymbol{\phi}^\intercal \boldsymbol{M} \right] \frac{d\boldsymbol{\phi}}{d\rho} \\ & + \left[\frac{\boldsymbol{\phi}^\intercal \frac{\partial \boldsymbol{G}}{\partial \boldsymbol{u}_\sigma} \boldsymbol{\phi}}{\boldsymbol{\phi}^\intercal \boldsymbol{K} \boldsymbol{\phi}} - \boldsymbol{\lambda}_1^\intercal \boldsymbol{K} + \boldsymbol{\lambda}_2^\intercal \frac{\partial \boldsymbol{G}}{\partial \boldsymbol{u}_\sigma} \boldsymbol{\phi} \right] \frac{d\boldsymbol{u}_\sigma}{d\rho} \end{aligned} \tag{24}$$

Here all terms multiplied with the derivative of $\boldsymbol{\phi}$ or $\boldsymbol{u}_\sigma$ have been grouped, as these are computationally expensive to evaluate. Values for the Lagrange multipliers must be determined which omit these terms from the calculation. This results in the following adjoint problems to be solved for $\boldsymbol{\lambda}_1$ and $\boldsymbol{\lambda}_2$:

$$\left(\boldsymbol{K} + \boldsymbol{G} - \omega^2 \boldsymbol{M} \right) \boldsymbol{\lambda}_2 = \left(-\frac{2}{\boldsymbol{\phi}^\intercal \boldsymbol{K} \boldsymbol{\phi}} \boldsymbol{G} + \frac{2\boldsymbol{\phi}^\intercal \boldsymbol{G} \boldsymbol{\phi}}{\left(\boldsymbol{\phi}^\intercal \boldsymbol{K} \boldsymbol{\phi} \right)^2} \boldsymbol{K} + 2\lambda_3 \boldsymbol{M} \right) \boldsymbol{\phi} \tag{25}$$

$$\boldsymbol{K} \boldsymbol{\lambda}_1 = \left(\frac{\boldsymbol{\phi}^\intercal}{\boldsymbol{\phi}^\intercal \boldsymbol{K} \boldsymbol{\phi}} + \boldsymbol{\lambda}_2^\intercal \right) \frac{\partial \boldsymbol{G}}{\partial \boldsymbol{u}_\sigma} \boldsymbol{\phi} \tag{26}$$

In equation (25), the matrix by which $\boldsymbol{\lambda}_2$ is multiplied is singular. In similar fashion to [29], the Lagrange multiplier $\boldsymbol{\lambda}_2$ is expressed as a linear combination of the mode shape $\boldsymbol{\phi}$ (multiplied by an arbitrary scalar c) and a 'particular solution' denoted as $\boldsymbol{\psi}$.

$$\boldsymbol{\lambda}_2 = c\boldsymbol{\phi} + \boldsymbol{\psi} \tag{27}$$

The solution to $\boldsymbol{\lambda}_2$ exists if and only if the right-hand-side term of problem (25) is orthogonal to $\boldsymbol{\phi}$ [29]. This statement can be verified by pre-multiplying all terms in (25) with $\boldsymbol{\phi}$, and by applying the definition given in (6). The first two terms on the right-hand-side will cancel each other, as $\frac{2\boldsymbol{\phi}^\intercal \boldsymbol{G}\boldsymbol{\phi}}{\boldsymbol{\phi}^\intercal \boldsymbol{K}\boldsymbol{\phi}} = \frac{\boldsymbol{\phi}^\intercal \boldsymbol{G}\boldsymbol{\phi} \cdot 2\boldsymbol{\phi}^\intercal \boldsymbol{K}\boldsymbol{\phi}}{(\boldsymbol{\phi}^\intercal \boldsymbol{K}\boldsymbol{\phi})^2}$. The only remaining term is $2\lambda_3\boldsymbol{M}$, which is equal to zero if and only if $\lambda_3 = 0$. *Note: In the sensitivity analysis by [29], a different objective function was analyzed which resulted in a non-zero value of their respective* λ_3. An expression for the particular solution $\boldsymbol{\psi}$ can now be found by solving the following system:

$$\left(\boldsymbol{K} + \boldsymbol{G} - \omega^2\boldsymbol{M}\right)\boldsymbol{\psi} = \left(-\frac{2}{\boldsymbol{\phi}^\intercal \boldsymbol{K}\boldsymbol{\phi}}\boldsymbol{G} + \frac{2\boldsymbol{\phi}^\intercal \boldsymbol{G}\boldsymbol{\phi}}{\left(\boldsymbol{\phi}^\intercal \boldsymbol{K}\boldsymbol{\phi}\right)^2}\boldsymbol{K}\right)\boldsymbol{\phi} \tag{28}$$

The system in (28) is singular, which means that infinitely many solutions exist. To find an approximate solution to the system, the algorithm developed by Ivo Babuška and colleagues was used [30, 31]. This algorithm transforms and perturbs the singular system, resulting in an extremely high condition number, but a non-singular system. An iterative algorithm finds a solution to the system (which only requires a single LU-factorization, making it computationally efficient). After determining $\boldsymbol{\psi}$, an arbitrary value for the scalar c can be chosen. In this project, it was chosen to satisfy the following equation:

$$\boldsymbol{\lambda}_2^\intercal \boldsymbol{M}\boldsymbol{\phi} = 0 \quad \Rightarrow \quad c = -\boldsymbol{\psi}^\intercal \boldsymbol{M}\boldsymbol{\phi} \tag{29}$$

Choosing this value for c omits the computation of $\frac{d\omega^2}{d\rho}$ in (24), which is computationally favorable. Now that the expression for $\boldsymbol{\lambda_2}$ is known, the problem stated in (26) can directly be solved for for $\boldsymbol{\lambda}_1$. Inserting the determined values for the Lagrange multipliers into (24) resulting the following expression for the objective sensitivity:

$$\frac{dL}{d\rho} = \frac{\boldsymbol{\phi}^\intercal \frac{\partial \boldsymbol{G}}{\partial \rho}\boldsymbol{\phi}}{\boldsymbol{\phi}^\intercal \boldsymbol{K}\boldsymbol{\phi}} - \frac{\boldsymbol{\phi}^\intercal \boldsymbol{G}\boldsymbol{\phi} \cdot \boldsymbol{\phi}^\intercal \frac{d\boldsymbol{K}}{d\rho}\boldsymbol{\phi}}{\left(\boldsymbol{\phi}^\intercal \boldsymbol{K}\boldsymbol{\phi}\right)^2} + \boldsymbol{\lambda}_1^\intercal\left(\frac{d\boldsymbol{f}_\sigma}{d\rho} - \frac{d\boldsymbol{K}}{d\rho}\boldsymbol{u}_\sigma\right) + \boldsymbol{\lambda}_2^\intercal\left(\frac{d\boldsymbol{K}}{d\rho} + \frac{\partial \boldsymbol{G}}{\partial \rho} - \omega^2\frac{d\boldsymbol{M}}{d\rho}\right)\boldsymbol{\phi} \tag{30}$$

C Finite Difference Check

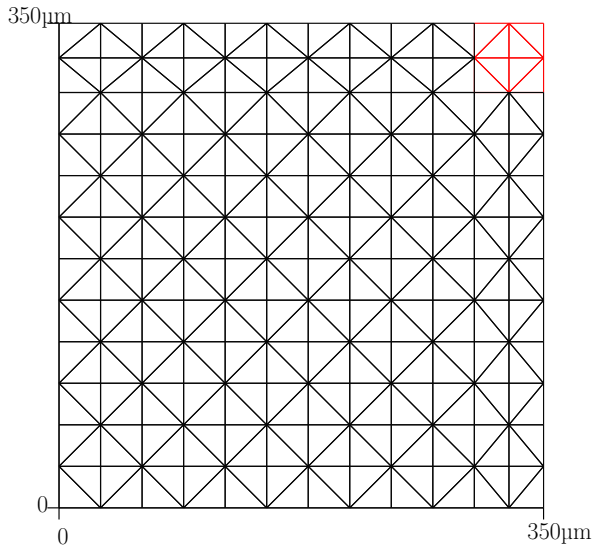

Figure 6: Mesh used for the finite difference (FD) verification of the objective function (eq. 8). Symmetry conditions were prescribed at the north and east boundaries. Fully clamped conditions were prescribed at the south and west boundaries. A fixed density of $\rho_e = 1$ was prescribed to all elements in the red region, as well as all elements in direct contact with the south and west border. In all other elements, a pseudo-random density between 0 and 1 was prescribed. The element type of choice was a T3 shell element, with a linearized formulation of [21]. All designs were evaluated at a thickness of 340nm with a prestress of 1.1GPa, imitating the values used in [9]. The material of choice was Si_3N_4, for which the material properties have been listed in Appendix D.

D Material properties of Si_3N_4

The values of these material properties correspond to those used in COMSOL, which is a commercial finite element package.

Property	**Symbol**	**Value**	**Unit**
Young's modulus	E	250	GPa
Poisson's ratio	ν	0.23	-
Mass density	ρ	3100	$\mathrm{kg\,m^{-3}}$

E Supporting simulation results

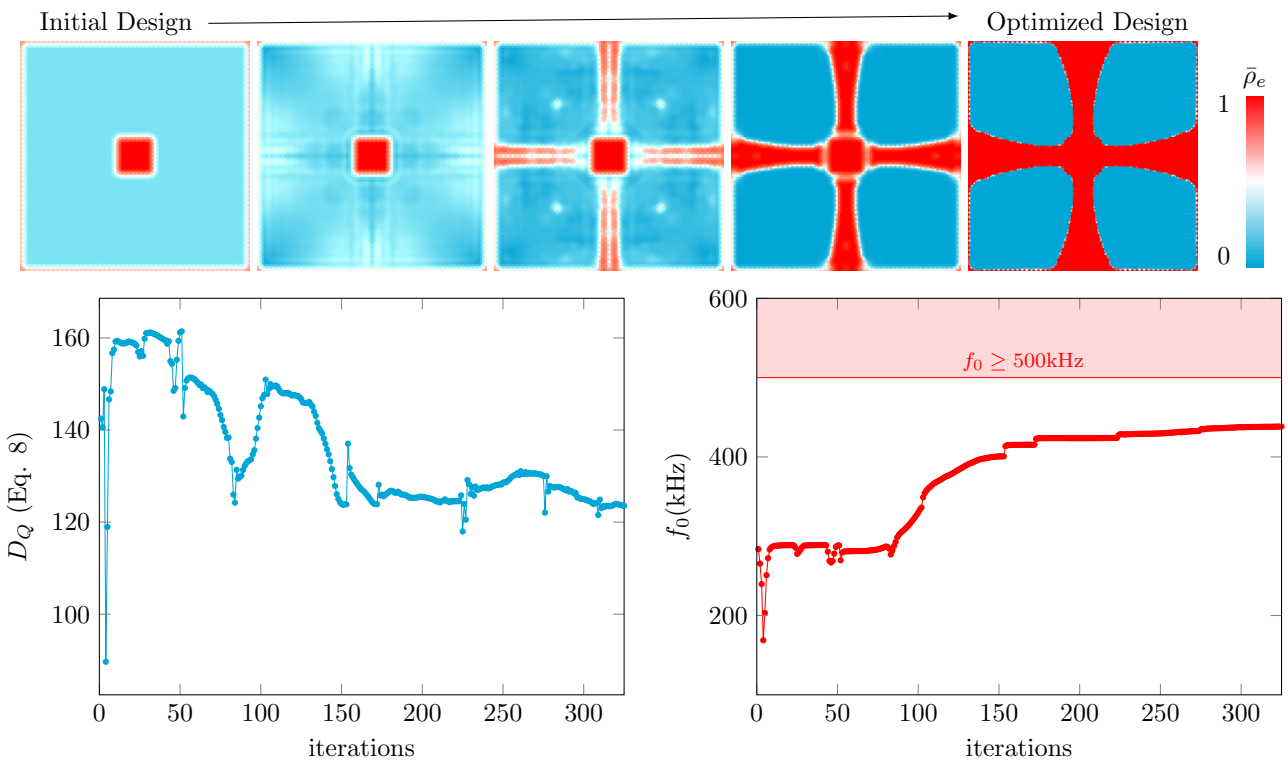

Figure 7: An optimization procedure with a frequency lower bound of 500kHz and a volumetric fraction of 0.2. The lower bound for the frequency constraint is too high in combination with the volumetric fraction, which results in frequency maximization study (instead of D_Q maximization). The final geometry strongly resembles the results obtained in [19], which concerned the frequency maximization of a prestressed plate structure with a non-structural mass placed at the center. These results highlight the importance of choosing a suitable combination of value for the prescribed frequency lower bound and volumetric fraction.

F Robust methodology

This section gives a brief overview of the robust optimization approach [28] which is commonly used to avoid dependency on intermediate density values in the optimization results. Due to the high computational cost and time constraints, this methodology was not successfully used in the final simulations. However, it is recommended for future studies as it allows for the frequency lower bound to be decreases whilst ensuring manufacturability and a level of connectedness to the boundaries of the system.

The robust method works by applying three different projections to the filtered densities, varying the threshold (central point) of the projection operation. This results in three projected designs, based on a single design vector. The performance of all three designs is evaluated, and the worst-performing design is selected. An example can be found in [20], where the projection threshold η in (11) was varied as $\eta \in [0.45, 0.50, 0.55]$. These three values for η result in the *dilated*, *intermediate* and *eroded* designs, respectively. The volume constraint is subsequently applied to the dilated design only, as it will always have the highest volumetric fraction. Furthermore, the frequency constraint is applied to every design separately (i.e., a unique frequency constraint for each design). The optimizer uses the sensitivities of the worst-performing design to determine its design update. Therefore, if intermediate design densities are beneficial to the objective function (which was found to be the case when maximizing dissipation dilution), the design that depends *the least* on intermediate values will generally be selected. A downside to this methodology is the associated increase in computational cost, as the problem and sensitivity analysis has to be executed in threefold for every iteration.

4

Nelson's Method for Computing Prestressed Eigenvector Gradients

This second manuscript is an independent addition to work of this thesis. In search of a way to accurately compute the gradient of the novel objective function presented in Chapter 3, an interesting idea was investigated which aimed to accurately compute the prestressed mode shape gradient $d\phi/d\rho_e$. The methodology presented in this additional manuscript uses a matrix of Lagrange multipliers to achieve this, which (to the author's best knowledge) is a novel technique. Even though this method is infeasible for use in the density-based topology optimization approach used in Chapter 3 (due to its high computational cost), it was still an interesting find and has been added to this thesis for good measure (and to demonstrate that not all work that is done directly contributes to the end goal of a thesis).

Nelson's Method for Computing Prestressed Eigenvector Gradients

H.J. Algra (5654890)

Abstract

Nelson's method is a well-established approach used to compute the sensitivity of eigenvectors with respect to a model's design parameters. This work extends the approach to include the effects of prestress, which adds a geometrically nonlinear relation between the design variables and eigenvectors. The proposed methodology employs a matrix of Lagrange multipliers to omit a computationally expensive term from the sensitivity analysis, which is subsequently verified by comparison to results from the finite difference method.

Keywords: *Nelson's method, prestressed eigenvectors, eigenvector gradients, adjoint sensitivity analysis*

Introduction

The computation of eigenfrequency and eigenvector sensitivities with respect to design parameters is required to update certain models, in optimization studies, fault detection and other applications [1]. Nelson's method [2] is a well-established technique for computing eigenvector sensitivities. This method has been extended by Lee et al. for damped systems with distinct [3] and multiple [4] eigenvalues. Furthermore, it has been extended for non-proportionally damped systems by [1] (for systems with complex modes) and by [5] (for second-order sensitivity analysis). This brief work extends the analytical sensitivity analysis of eigenvectors for undamped prestressed systems, in which geometric nonlinearity needs to be taken into account.

Theoretical Foundation

A. Prestressed Analysis

The stiffness properties of mechanical structures can be strongly influenced by the presence of (pre)stress. As a result of the stiffness change, both the eigenfrequencies and eigenvectors are affected as well. This work investigates how eigenvector gradients can be accurately computed when dealing with prestressed systems. In these systems, the tangent stiffness matrix has an additional contribution based on the static stress state (known as the geometric stiffness). This results in the following eigenvalue problem:

$$\left(\boldsymbol{K}_t + \boldsymbol{G} - \omega_i^2 \boldsymbol{M}\right) \boldsymbol{\phi}_i = \boldsymbol{0} \tag{1}$$

The overall tangent stiffness matrix of the system is defined as $\boldsymbol{K}_t \equiv \boldsymbol{K} + \boldsymbol{G}$. Together with mass matrix $\boldsymbol{M}$ it is used to compute the eigenfrequencies ω^2 and eigenvectors $\boldsymbol{\phi}$. It is assumed that $\boldsymbol{K}$ directly depends on system parameters s_i. Conversely, the geometric stiffness matrix has an additional dependence on the design parameters, as it is influenced the static displacements $\boldsymbol{u}_\sigma$. In other words, the dependency of the stiffness matrices can expressed as $\boldsymbol{K} \equiv \boldsymbol{K}(s_i)$ and $\boldsymbol{G} \equiv \boldsymbol{G}(\boldsymbol{u}_\sigma(s_i), s_i)$.

After solving the modal system defined in (1), a common practice is to normalize the magnitude of the eigenvectors with respect to the mass matrix. This is expressed in the equation below.

$$\boldsymbol{\phi}_i^\intercal \boldsymbol{M} \boldsymbol{\phi}_i = 1 \tag{2}$$

For the sensitivity of prestressed eigenvalues, the reader is referred to [6]. Furthermore, as the proposed methodology is independent of the index of the eigenmode, the subscript is dropped for the further of this work for clarity.

B. Prestressed Eigenmode Gradients

The sensitivities of eigenvectors can be computed using Nelson's method [2]. A summary of this method can be found in [3]. Its fundamental principle is the expression of the eigenvector gradient in terms of the eigenmode and a particular solution, which is given below.

$$\frac{d\boldsymbol{\phi}}{ds_i} = c\boldsymbol{\phi} + \boldsymbol{\psi} \tag{3}$$

Here, c is an arbitrary constant which multiplies the homogeneous part of the solution and $\boldsymbol{\psi}$ represents the unknown particular solution. Nelson's method differentiates the eigenvalue problem (1) with respect to a design variable s_i, after which expressions are found for c and $\boldsymbol{\psi}$. Due to the dependency of the geometric stiffness $\boldsymbol{G}$ on the static displacements $\boldsymbol{u}_\sigma$, the derivative of (1) will result in a term that contains $\frac{d\boldsymbol{u}_\sigma}{ds_i}$. The computation of this term is expensive, and can be omitted by augmenting the problem with the constitutive static analysis. This is done by using a matrix of Lagrange multipliers, which

is denoted as $\boldsymbol{\Lambda}$ below.

$$\left(\boldsymbol{K}+\boldsymbol{G}-\omega^2\boldsymbol{M}\right)\boldsymbol{\phi}+\boldsymbol{\Lambda}^{\intercal}\left(\boldsymbol{f}_{\sigma}-\boldsymbol{K}\boldsymbol{u}_{\sigma}\right)=\boldsymbol{0} \tag{4}$$

Differentiating (4) with respect to s_i, and regrouping terms multiplied with $\frac{d\boldsymbol{u}_\sigma}{ds_i}$ results in

$$\begin{aligned}\left(\boldsymbol{K}+\boldsymbol{G}-\omega^2\boldsymbol{M}\right)\frac{d\boldsymbol{\phi}}{ds_i}=&-\left(\frac{d\boldsymbol{K}}{ds_i}+\frac{\partial\boldsymbol{G}}{\partial s_i}-\omega^2\frac{d\boldsymbol{M}}{ds_i}\right)\boldsymbol{\phi}\\&-\boldsymbol{\Lambda}^{\intercal}\left(\frac{d\boldsymbol{f}_\sigma}{ds_i}-\frac{d\boldsymbol{K}}{ds_i}\boldsymbol{u}_\sigma\right)\\&+\frac{d\omega^2}{ds_i}\boldsymbol{M}\boldsymbol{\phi}\\&+\left[\boldsymbol{\Lambda}^{\intercal}\boldsymbol{K}-\frac{\partial\boldsymbol{G}}{\partial\boldsymbol{u}_\sigma}\boldsymbol{\phi}\right]\frac{d\boldsymbol{u}_\sigma}{ds_i}.\end{aligned} \tag{5}$$

In order to omit the computation of $\frac{d\boldsymbol{u}_\sigma}{ds_i}$ from this expression, the expression between square brackets is equated to zero. This requires the following linear problem to be solved for $\boldsymbol{\Lambda}$:

$$\boldsymbol{K}\boldsymbol{\Lambda}=\boldsymbol{\phi}^{\intercal}\frac{\partial\boldsymbol{G}}{\partial\boldsymbol{u}_\sigma} \tag{6}$$

After solving (6) for the matrix $\boldsymbol{\Lambda}$, the following problem must be solved to determine the particular solution:

$$\begin{aligned}\left(\boldsymbol{K}+\boldsymbol{G}-\omega^2\boldsymbol{M}\right)\boldsymbol{\psi}=&-\left(\frac{d\boldsymbol{K}}{ds_i}+\frac{\partial\boldsymbol{G}}{\partial s_i}-\omega^2\frac{d\boldsymbol{M}}{ds_i}\right)\boldsymbol{\phi}\\&+\frac{d\omega^2}{ds_i}\boldsymbol{M}\boldsymbol{\phi}-\boldsymbol{\Lambda}^{\intercal}\left(\frac{d\boldsymbol{f}_\sigma}{ds_i}-\frac{d\boldsymbol{K}}{ds_i}\boldsymbol{u}_\sigma\right)\end{aligned} \tag{7}$$

In (7) the matrix by which $\boldsymbol{\psi}$ is multiplied is singular. In the original method presented by Nelson, [2, 3], this system is made non-singular by enforcing the k-th entry of (3) to be zero. Here k indicates the entry of $\boldsymbol{\phi}$ such that $\boldsymbol{\phi}[k]=\texttt{max}[\boldsymbol{\phi}]$. An alternative approach is to use an algorithm developed by Ivo Babuška and colleagues [7, 8], which seeks an approximate solution to the singular system at hand. Both methods can be used to find an approximate solution to the system, and will be used in this work.

It should be noted that infinitely many solutions exist for singular systems, and that both approaches will result in an approximation of a non-unique solution to the system. Therefore, the value of the arbitrary scalar c must be carefully chosen to ensure a valid result. This value is found by differentiating (2), which results in:

$$2\boldsymbol{\phi}^{\intercal}\boldsymbol{M}\frac{d\boldsymbol{\phi}}{ds_i}+\boldsymbol{\phi}^{\intercal}\frac{d\boldsymbol{M}}{ds_i}\boldsymbol{\phi}=0 \tag{8}$$

Inserting the definition for the eigenvector gradient (3) into (8) results in an expression for the unknown scalar c, which reads:

$$c=-\boldsymbol{\phi}^{\intercal}\boldsymbol{M}\boldsymbol{\psi}-0.5\boldsymbol{\phi}^{\intercal}\frac{d\boldsymbol{M}}{ds_i}\boldsymbol{\phi} \tag{9}$$

It is worth noting that the definition for eigenfrequency sensitivities (derivation given in [6]) can be retrieved by inserting the homogeneous part of the mode shape $\left(\frac{d\boldsymbol{\phi}}{ds_i}=c\cdot\boldsymbol{\phi}\right)$ into (5), and pre-multiplying all terms by $\boldsymbol{\phi}^{\intercal}$. This results in the following expression:

$$\begin{aligned}\frac{d\omega^2}{ds_i}=&\boldsymbol{\phi}^{\intercal}\left(\frac{d\boldsymbol{K}}{ds_i}+\frac{\partial\boldsymbol{G}}{\partial s_i}-\omega^2\frac{d\boldsymbol{M}}{ds_i}\right)\boldsymbol{\phi}\\&+\boldsymbol{\phi}^{T}\boldsymbol{\Lambda}^{\intercal}\left(\frac{d\boldsymbol{f}_\sigma}{ds_i}-\frac{d\boldsymbol{K}}{ds_i}\boldsymbol{u}_\sigma\right)\end{aligned} \tag{10}$$

Here the following adjoint problem must be solved for the vector of Lagrange multipliers inherent to the eigenfrequency sensitivity problem, which can be defined as $\boldsymbol{\mu}\equiv\boldsymbol{\Lambda}\boldsymbol{\phi}$:

$$\boldsymbol{K}\boldsymbol{\mu}=\boldsymbol{\phi}^{\intercal}\frac{\partial\boldsymbol{G}}{\partial\boldsymbol{u}_\sigma}\boldsymbol{\phi}. \tag{11}$$

Numerical Verification

The proposed method of computing eigenvector gradients was analyzed in the context of topology optimization [9]. In this technique, the design parameters concern a penalization of the local Young's modulus and mass density of every element. The following sample objective function was analyzed:

$$f_{obj}=\boldsymbol{\phi}^{\intercal}\boldsymbol{\phi} \tag{12}$$

The differentiation of this objective with respect to a design parameter s_i is trivial, and reads:

$$\frac{df_{obj}}{ds_i}=2\boldsymbol{\phi}^{\intercal}\frac{d\boldsymbol{\phi}}{ds_i} \tag{13}$$

For a plate system with prestress, the prestressed eigenmodes and their gradients were computed with the approach described in the previous section. The verification of the proposed method was carried out by computing the relative difference between the analytical sensitivity (13) and sensitivities obtained with finite differences (FD). For the analytical sensitivity two approaches were used. The first was the approach is typical for Nelson's method, which prescribes one component of the eigenvector gradient to be zero [3] (the index of this component corresponds to the largest component of the eigenmode itself). As an alternative, Babuška's algorithm for singular systems [7, 8] was also looked into. The relative difference between the analytical and FD sensitivities has been plotted in Figures 1 and 2.

For both methods the minimum relative difference was found at a step size of 5×10^{-5}, corresponding to relative difference in the order of 10^{-8}. The accuracy is comparable to the accuracy of a static compliance minimization objective, of which the sensitivities are well-known and extremely accurate. This validates the correctness of the proposed approach used to compute $d\boldsymbol{\phi}/d\rho_e$. Furthermore, both approaches of solving the singular system 7 perform similarly, indicating that both methods can be used to solve singular systems.

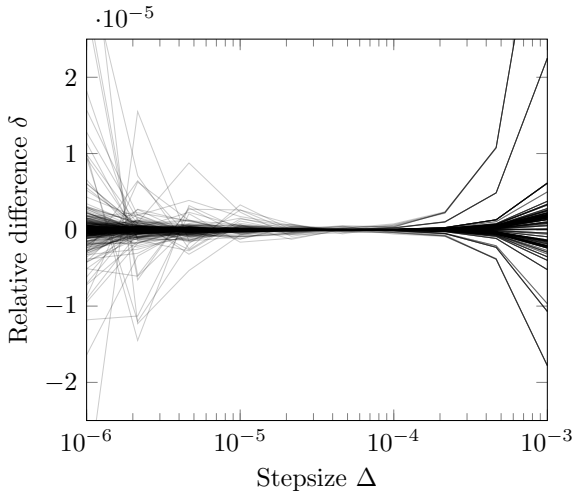

Figure 1: Finite Difference Check using Nelson's approach of zeroing out the k-th eigenvector gradient entry to solve the singular system in (7).

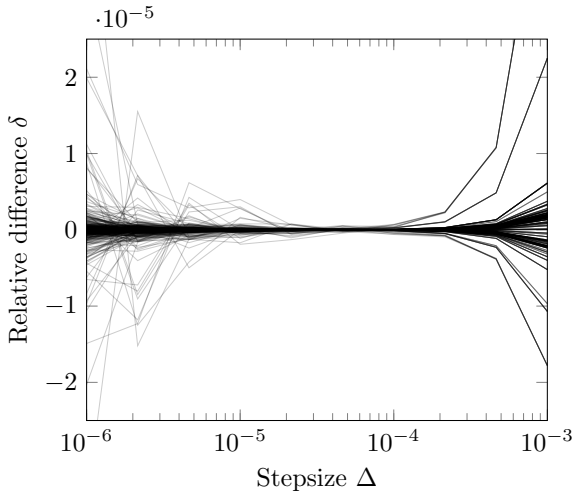

Figure 2: Finite Difference Check using Babuška's algorithm to solve the singular system in (7).

Discussion

Nelson's method is an approach used to compute eigenvector gradients in modal problems. This work extends the method to undamped systems in which prestress is present. These systems contain a geometric stiffness matrix, which has both a direct and indirect dependence on the design variables (through a dependence on the equilibrium stress configuration). A novel approach of using a matrix of Lagrange multipliers was used to omit the calculation of this dependence through adjoint sensitivity analysis. The work was verified by applying finite difference checks to a topology optimization problem, of which the sensitivities required the computation of the mode shape gradient. The results show a very good correlation between the analytical sensitivities (computed using the analytical approach in this paper) and the finite difference sensitivities, which an accuracy comparable to the well-known compliance minimization problem. This validates the validity of the proposed method.

A downside to the calculation of mode gradients in general is the associated computational cost, which is severe for problems with a large number of degrees of freedom. This is why the mode gradient term is often omitted from the sensitivity analysis altogether if it is possible to do so. The computational expense stems from the fact that the each element's eigenmode gradient depends on all design variables. Therefore, a system of equations must be solved to compute $d\phi/d\rho$ for every element, which explains the practice of omitting the computation of the mode gradient from the analysis altogether. Nevertheless, the method proposed in this work provides a way of computing this term, which could be useful for other optimization problems (i.e., with less design variables or problems in which the mode gradient cannot be omitted). Furthermore, it demonstrates the use of Lagrange multipliers in a matrix-form, which is novel and could be interesting for other optimization problems as well.

References

[1] S. Adhikari M. Friswell. "Derivatives of Complex Eigenvectors Using Nelson's Method". In: *Aerospace Research Central* 38.12 (2000), pp. 2355–2356. DOI: 10.2514/2.907.

[2] Richard B. Nelson. "Simplified calculation of eigenvector derivatives". In: *AIAA Journal* 14.9 (1976). DOI: 10.2514/3.7211.

[3] G. Jung I. Lee D. Kim. "An efficient algebraic method for the computation of natural frequency and mode shape sensitivities—Part I. Distinct natural frequencies". In: *Computers & Structures* 223.3 (1999), pp. 399–412. DOI: 10.1006/jsvi.1998.2129.

[4] G. Jung I. Lee D. Kim. "An efficient algebraic method for the computation of natural frequency and mode shape sensitivities—Part I. Distinct natural frequencies". In: *Computers & Structures* 223.3 (1999), pp. 413–424. DOI: 10.1006/jsvi.1998.2130.

[5] H. Smaoui N. Guedriaa M. Chouchaneb. "Second-order eigensensitivity analysis of asymmetric damped systems using Nelson's method". In: *Journal of Sound and Vibration* 300 (2007), pp. 974–992. DOI: 10.1016/j.jsv.2006.09.003.

[6] N.L. Pedersen. "On topology optimization of plates with prestress". In: *International Journal for Numerical Methods in Engineering* 51 (2001), pp. 225–239. DOI: 10.1002/nme.162.

[7] J.T. Oden C.A. Duarte I. Babuška. "Generalized finite element methods for three-dimensional structural mechanics problems". In: *Computers & Structures* 77.2 (2000), pp. 215–232. DOI: 10.1016/S0045-7949(99)00211-4.

[8] Alejandro M. Aragón and C. Armando Duarte. *Fundamentals of Enriched Finite Element Methods*. 1st ed. ISBN: 9780323855150. Elsevier, 2023.

[9] M.P. Bendsøe and O. Sigmund. *Topology Optimization Theory, Methods and Applications*. 1st ed. Springer, 2004. DOI: 10.1007/978-3-662-05086-6.

5 Conclusion & Outlook

The goal of this thesis was to apply structural optimization techniques to enhance the quality factor of nanomechanical structures, without a dependency on *a priori* information from the user. From literature, it is known that the geometric design of a structure and its Q factor are related through an effect called dissipation dilution, which captures the effect of tensile stress on the stored and dissipated energy during oscillation. In this work, a simple formula was proposed to model this effect, based on the material and geometric stiffness matrices of a finite element model. An excellent correlation between the proposed formula and the "traditional" (more complex) formula was found. In order to employ the novel formula as an objective for topology optimization (TO), the adjoint method was used to determine its sensitivity with respect to element-level design parameters. The identification of this formula and its sensitivity are unique and novel contributions of this thesis. The primary advantage of optimizing for this equation is that no *a priori* knowledge is required (e.g., experimental data or a parameterized design). This adds versatility to the optimization framework, as it can be applied to situations with different materials or geometric parameters. Another advantage of using the novel formula is that it is considerably more simple to compute, in comparison to the 'traditional' one (e.g., as used in [8]). Furthermore, the adjoint sensitivity analysis used to compute the gradients of this function was relatively complicated, due to the presence of prestress and the singular modal system. Computing sensitivities that depend on prestressed systems [31] or singular matrices [32] has been done in the past, but to the author's best knowledge this thesis is the first work that combines the two.

The final optimization work was aimed to be a proof of concept, as TO studies are only quantitatively comparable when exactly the same optimization parameters (i.e., constraints and penalization/projection/filtering schemes) [33]. In this work, the setup used by a Q factor TO study found in literature [11, 30] was imitated, albeit for a different membrane thickness, filter radius and element type. Nevertheless, similar resonator designs were found which qualitatively indicates that the proposed approach is comparable to those found in literature. It should be emphasized that achieving a "nice" black-and-white design when working with density-based TO is by no means an easy task, which is a process that requires experience as well as a bit of educated guessing. In essence, the difficulty lies in the construction of the optimization problem itself, as *every* change made to the projection, penalization, constraints etc. inherently changes the problem that is being solved. In literature, the way in which the final problem was set up is commonly stated, but rarely explained. This gives an incomplete view of the process that the other authors went through to end up at their final results, which complicates both understanding as well as solving the optimization problem.

The implemented and verified methodology has paved a pathway to a wide range of future studies. First of all, the problem of designing trampolines can be looked into further. Improvements such as a finer mesh and stability at lower thicknesses can result in accurate designs with possibly extremely high Q factors. It observed that the values of the corresponding constraints and initial geometries is a important aspect of this study, which is something that can be investigated further as well.

On the next page a concise summary of the opportunities for future research is given.

An investigation into whether resonators with even higher Q factors or $Q \times f_0$ products can be designed. One of the observations made during the relatively short optimization study at the end of Chapter 3, was the the optimization problem itself is quite non-convex. The penalization/projection/filtering schemes, as well as the constraint values and initial material distribution all influence the geometry and performance of the final structure. By testing and comparing different ways of setting up the optimization problem, a better understanding of the problem altogether can be obtained, which can be beneficial to finding 'better' designs. In TO there is no guarantee that a design is the global, so it is advantageous to study different problem configurations and see what their effects are on the overall optimization procedure. *The reader is referred to [33] for an in-depth discussion of density-based TO results, and how comparisons can be made*. Furthermore, working with finer meshes (requiring an increase in the available computational resources) could prove to be beneficial, as it it can be used to create finer designs. It should be noted that the work that was used as a reference for this paper [30], used an extremely fine mesh, in which the filter covered 9 elements. The effect of the mesh size on the designs and their fidelity is another interesting aspect to be explored. Finally, the dilution factor of structures is commonly seen to inversely scale with their thickness, which incentivizes adding support for thinner membranes (e.g. $50\mathrm{nm}$). In the current implementation, this thickness was observed to result in an unstable optimization procedure. Finally, the "Robust Method" was implemented and verified, but not used due to time constraints. Using this approach is highly recommended for future work.

Designs obtained in this (and future) work can be validated experimentally. The performance of resonator designs presented in the main work of this thesis has only been verified numerically. Experimental verification (e.g. by means of fabrication followed by a ringdown experiment) of the dissipation dilution equation presented in this work should be conduced to gain further insight into the accuracy of the proposed equation. This could also shed light on the fundamental validity of the equation itself, as other damping mechanisms also affect the Q factor of a structure (i.e., under what conditions or geometries is the equation accurate/inaccurate).

In order to deepen the understanding of prestressed resonating structures in general, the methodology could be used to design resonators for other geometries. Designing resonators in triangle, circle or hexagon shapes could lead to new insights into the interplay between geometry, dissipation dilution and the Q factor of structures in general. A common phenomenon observed in nanomechanical resonators is the trade-off between fundamental frequency and Q factor. Investigating what other trade-offs are made, or whether certain aspects can be circumvented is another interesting path of research. For example, studying the relation between the amount of material present in the domain (volumetric fraction) and the overall fundamental frequency, Q factor or $Q \times f_0$ product could be an interesting topic to look into.

A different optimization methodology could be used in comparison to the current implementation. In density-based TO, intermediate density values are problematic and difficult to mitigate. Therefore, the use of a level-set based method (LSM) could be beneficial to the optimization problem at hand. The current density-based implementation can serve as a frame of reference, as well as a proof of concept for the objective at hand. Although the use of the LSM approach does not seem to be as widespread compared to density-based TO, it is definitely a strong competitor. A major advantage of this technique is that it inherently mitigates the any dependency on intermediate density values, as its designs have well-defined geometric boundaries. *The reader is referred to [34] for an advanced implementation of this technique.*

The use of artificial intelligence to classify and design high-Q resonators. A major current topic, both in and out of the academic world, is the use of artificial intelligence. In a recent study by [35], deep learning was used to predict the properties of micromechanical resonator designs. The speed of the design classifications (that did not use FEM) allowed for a non-parameterized optimization study, using a structural generator (this optimization technique was not gradient-based). A similar study could be conducted on the resonators in question in this paper. It should be noted that presence of prestress will complicate the classification analysis, as it adds a strong nonlinearity to the relation between the geometry of a structure and its dynamic performance. Nevertheless, investigating the use of artificial intelligence to optimize prestressed nanomechanical structures is definitely a worthwhile operation and makes for a very interesting topic of future research.

References

[1] C. Mauran. *Mashable*. 2022. URL: https://mashable.com/article/apple-iphone-crash-detection-how-it-works (visited on 10/04/2023).

[2] H.J. Mamin and D. Rugar. "Sub-attonewton force detection at millikelvin temperatures". In: *Applies Physics Letters* 79.3358 (2001). DOI: 10.1063/1.141825.

[3] Thomas Burg, Michel Godin, Scott Knudsen, Wenjiang Shen, Greg Carlson, John Foster, Ken Babock, and Scott Manalis. "Weighing of biomolecules, single cells and single nanoparticles in fluid". In: *Nature* 446 (2007), pp. 1066–1069. DOI: 10.1038/nature05741.

[4] J. Chaste, A. Eichler, J. Moser, G. Ceballos, R. Rurali, and A. Bachtold. "A nanomechanical mass sensor with yoctogram resolution". In: *Nature Nanotechnology* 7 (2012), pp. 301–304. DOI: 10.1038/NNANO.2012.42.

[5] A. O'Connell, M. Hofheinz, M. Ansmann, R. Bialczak, M. Leander, E. Lucero, M. Neeley, D. Sank, H. Wang, M. Weides, J. Wenner, J. Martinis, and A. Cleland. "Quantum ground state and single-phonon control of a mechanical resonator". In: *Nature* 464 (2010), pp. 697–703. DOI: 10.1038/nature08967.

[6] R. Norte, J. Moura, and S. Gröblacher. "Mechanical Resonators for Quantum Optomechanics Experiments at Room Temperature". In: *Phyical Review Letters* 116.147202 (2016). DOI: 10.1103/PhysRevLett.116.147202.

[7] S. Fedorov. "Mechanical resonators with high dissipation dilution in precision and quantum measurements". PhD thesis. École Polytechnique Fédérale de Lausanne, Jan. 2021.

[8] D. Shin, A. Cupertino, M. De Jong, P. Steeneken, and M. Bessa. "Spiderweb Nanomechanical Resonators via Bayesian Optimization: Inspired by Nature and Guided by Machine Learning". In: *Advanced Materials* 34.3 (2021). DOI: 10.1002/adma.202106248.

[9] Z. Li, M. Xu, R. Norte, F. Alijani, A. Aragón, F. van Keulen, and P. Steeneken. "Tuning the Q-factor of Nanomechanical String Resonators by Torsion Support Design". In: *Applied Physics Letters* 122.1 (2023). DOI: 10.1063/5.0133177.

[10] S. Schmid, K. D. Jensen, K. H. Nielsen, and A. Boisen. "Damping mechanisms in high-Q micro and nanomechanical string resonators". In: *Phys. Rev. B* 84 (16 2011), p. 165307. DOI: 10.1103/PhysRevB.84.165307.

[11] D. Høj. "Development of ultra-high quality mechanical oscillators". PhD thesis. Department of Physics, Technical University of Denmark, 2021.

[12] M.L. Roukes S. Schmid L.G. Villanueva. *Fundamentals of Nanomechanical Resonators*. 1st ed. Springer, 2016. ISBN: 978-3-319-28689-1. DOI: 10.1007/978-3-319-28691-4.

[13] M.A.G. Suijlen, J. Koning, M. Van Gils, and H. Beijerink. "Squeeze film damping in the free molecular flow regime with full thermal accommodation". In: *Sensors and Actuators* 156.1 (2009), pp. 171–179. DOI: 10.1016/j.sna.2009.03.025.

[14] Quirin P. Unterreithmeier, Thomas Faust, and Jörg P. Kotthaus. "Damping of Nanomechanical Resonators". In: *Phys. Rev. Lett.* 105 (2 2010), p. 027205. DOI: 10.1103/PhysRevLett.105.027205.

[15] S. Olcum, N. Cermak, S. Wasserman, K. Payer, W. Shen, J. Lee, and S. Manalis. "Suspended Nanochannel Resonators at Attogram Precision". In: *2014 IEEE 27th International Conference on Micro Electro Mechanical Systems (MEMS)* (2014). DOI: 10.1109/MEMSYS.2014.6765587.

[16] P. Sadeghi, M. Tanzer, S. Christensen, and S. Schmid. "Journal of Applied Physics". In: *Influence of clamp-widening on the quality factor of nanomechanical silicon nitride resonators* 126.165108 (2019). DOI: 10.1063/1.5111712.

[17] A. H. Ghadimi, D. Wilson, and T. Kippenberg. “Radiation and Internal Loss Engineering of High-Stress Silicon Nitride Nanobeams”. In: *Nano Letters* 17 (2017), pp. 3501–3505. DOI: 10.1021/acs.nanolett.7b00573.

[18] S. Fedorov, A. Beccari, N. Engelsen, and T. Kippenberg. “Fractal-like Mechanical Resonators with a Soft-Clamped Fundamental Mode”. In: *Physical Review letters* 124.025502 (2020). DOI: 10.1103/PhysRevLett.124.025502.

[19] A. Beccari, D. Visani, S. Fedorov, M. Beryehi, V. Boureau, N. Engelsen, and T. Kippenberg. “Strained crystalline nanomechanical resonators with quality factors above 10 billion”. In: *Nature Physics* 18 (2022), pp. 436–441. DOI: 10.1038/s41567-021-01498-4.

[20] J. Rodriguez, S. Chandorkar, C. Watson, G. Glaze, C. Ahn, E. Ng, Y. Yang, and T. Kenny. “Direct Detection of Akhiezer Damping in a Silicon MEMS Resonator”. In: *Scientific Reports* 9.224 (2019). DOI: 10.1038/s41598-019-38847-6.

[21] S. Verbridge, D. Shapiro, H. Craighead, and J. Parpia. “Macroscopic Tuning of Nanomechanics: Substrate Bending for Reversible Control of Frequency and Quality Factor of Nanostring Resonators”. In: *Nano Letters* 7.6 (2007), pp. 1728–1735. DOI: 10.1021/nl070716t.

[22] S. Fedorov, N. Engelsen, A. Ghadimi, M. Bereyhi, R. Schilling, D. Wilson, and T. Kippenberg. “Generalized dissipation dilution in strained mechanical resonators”. In: *Physical Review Letters* 99.054107 (2019). DOI: 10.1103/PhysRevB.99.054107.

[23] J.R. Pratt, A. Agrawal, C. Condos, C. Pluchar, S. Sclamminger, and D. Wilson. “Nanoscale Torsional Dissipation Dilution for Quantum Experiments and Precision Measurement”. In: *American Physical Society* 13.011018 (2023). DOI: 10.1103/PhysRevX.13.011018.

[24] Y. Tsaturyan, A. Barg, E. Polzik, and A. Schliesser. “Ultracoherent nanomechanical resonators via soft clamping and dissipation dilution”. In: *Nature Nanotechnology* 12 (2017), pp. 776–784. DOI: 10.1038/NNANO.2017.101.

[25] A. Beccari, M. Beryehi, R. Groth, S. Fedorov, A. Arabmohegi, T. Kippenberg, and N. Engelsen. “Hierarchical tensile structures with ultralow mechanical dissipation”. In: *Nature Communications* 13.3097 (2021). DOI: 10.1038/s41467-022-30586-z.

[26] M. J. Bereyhi, A. Beccari, S. Fedorov, A. Ghadimi, R. Schilling, D. Wilson, N. Engelsen, and T. Kippenberg. “Clamp-Tapering Increases the Quality Factor of Stressed Nanobeams”. In: *Nano Letters* 19 (2019), 2329−2333. DOI: 10.1021/acs.nanolett.8b04942.

[27] T. Gisler, M. Helal, D. Sabonis, U. Grob, M. Hénritier, C. Degen, A. Ghadimi, and A. Eichler. “Soft-Clamped Silicon Nitride String Resonators at Millikelvin Temperatures”. In: *Physical Review Letters* 129.104301 (2022). DOI: 10.1103/PhysRevLett.129.104301.

[28] V. J. Gokhale and Jason J. Gorman. “Approaching the intrinsic quality factor limit for micromechanical bulk acoustic resonators using phononic crystal tethers”. In: *Applied Physics Letters* 111.013501 (2017). DOI: 10.1063/1.4990960.

[29] D. Høj, F. Wang, W. Gao, U. Hoff, O. Sigmund, and U. Andersen. “Ultra-coherent nanomechanical resonators based on inverse design”. In: *Nature Communications* 12.5766 (2021). DOI: 10.1038/s41467-021-26102-4.

[30] W. Gao, F. Wang, and O. Sigmund. “Systematic design of high-Q prestressed micro membrane resonators”. In: *Computer Methods in Applied Mechanics and Engineerig* 361.112692 (2020). DOI: 10.1016/j.cma.2019.112692.

[31] N.L. Pedersen. “On topology optimization of plates with prestress”. In: *International Journal for Numerical Methods in Engineering* 51 (2001), pp. 225–239. DOI: 10.1002/nme.162.

[32] T. Tsai and C. Cheng. “Structural design for desired eigenfrequencies and mode shapes using topology optimization”. In: *Structural Multidisciplinary Optimization* 27 (2013), pp. 673–686. DOI: 10.1007/s00158-012-0840-2.

[33] O. Sigmund. “On benchmarking and good scientific practise in topology optimization”. In: *Structural and Multidisciplinary Optimization* 65.315 (2022). DOI: 10.1007/s00158-015-1372-3.

[34] S. Van den Boom, J. Zhang, A. Aragón, and F. Van Keulen. “An interface-enriched generalized finite element method for level set-based topology optimization”. In: *Structural And Multidisciplinary Optimization* 63 (2021), pp. 1–20. DOI: 10.1007/s00158-020-02682-5.

[35] R. Guo, F. Sui, W. Yue, Z. Wang, S. Pala, K. Li, Renxiao Xu, and L. Li. “Deep learning for non-parameterized MEMS structural design”. In: *Microsystems & Nanoengineering* 8.91 (2022). DOI: 10.1038/s41378-022-00432-9.

A

Project Time Management

Literature Review: February - April 2023

This project started off with an extensive literature survey, focusing on the fundamentals of nanomechanical resonators and their Q factors. The review first focused on the damping mechanisms that can affect the Q factor, as well as certain designs that aim to mitigate specific damping sources. It was observed that human intuition had been the main source of innovation when it came to designing high-Q resonators, and optimization techniques had not been applied extensively. This led to the identified research gap, which was the use of structural optimization techniques to enhance nanomechanical Q factors, using a method that did not depend on prior experimental or parameterized information. The goal stated at the end of the literature review in was threefold, and has been repeated below.

- Identify and implement a suitable optimization methodology for enhancing the Q factor of nanomechanical resonators.
- Use this methodology to design support structures that result in maximum Q factors.
- Verify the optimized designs by means of testing and experiments. *This last goal was not met due to time constraints.*

COMSOL Testing: May - June 2023

Initially, the option of using the Topology Optimization module in COMSOL was investigated, starting with the internal optimization module. However, it was determined that COMSOL does not support gradient-based optimization techniques for multi-step problems. In order to circumvent this problem, the option of analyzing the structure in COMSOL, and computing the gradients & doing the optimization with MATLAB (using LiveLink, which couples these two softwares) was also looked into. However, the process of extracting quantities required to do the sensitivity analysis in MATLAB can be classified as non-trivial at best (as few complicated workarounds were required to extract element volumes and stiffness matrices using LiveLink). In the end, the advantages of COMSOLs user-friendly interface were overshadowed by the complications encountered when extracting element-level quantities in LiveLink (which is not what this program was intended for). Therefore, the option of using COMSOL was disregarded for optimization purposes.

Hybrida: July 2023 - January 2024

In order to continue with Topology Optimization, it was decided that the department's in-house FEM package would be used. This package is named `Hybrida` and is courtesy of Professor A. Aragón. Working in `Hybrida` directly gives access to all aspects of the FEA involved, but also required a deeper understanding of the method used, as well as its implementational aspects. Furthermore, a few important functionalities which required implementation, such as prestressed static and modal analysis, support for shell elements in the existing optimization framework, as well as the sensitivity analysis required. A time-consuming aspect was correctly implementing the sensitivity analysis for eigenfre-

quency and “Q factor” optimization, the latter requiring a complicated adjoint analysis. Furthermore, implementing other aspects such as a projection function on top of the filtering procedure, automatic plotting features and support for vectorized elements (within the optimization framework) all took quite some time (as they also required a thorough understanding of the code). Quite some code developed by previous users was commented and improved, and an extremely long list of bugs has been fixed. An overview of the features added to the code has been added in Appendix B.

Simulations & Report: December 2023 - February 2024

After all features were implemented and verified, the optimization could begin. This involved a lot of trial and error, as many factors can influence the optimization results. Certain aspects such as the minimum density allowed in the design, and the type of penalization/projection functions used essentially change the nature of the optimization problem, and can result in completely different results. This part of the project overlapped with the implementational part preceding it, as the need for certain unimplemented features came to light when doing simulations. In addition to this, the introductory and theoretical sections of the thesis were mainly written in parallel to the simulations, which proved to be a productive use of the simulation time.

B

Contributions To `Hybrida`

Prestressed Eigenfrequency Analysis with Shells

- `tri_s3Lps` elements were added, which are linear shells that support prestressed analysis.
- Computing the derivative of the geometric stiffness matrix with respect to the static displacement was aded in `hybrid.get_dGdu()`.
- `Prestress` boundary condition has been added as an extension of `NeumannDistributed`. The actual contribution to the force vector is included in the element assembly of `s3Lps`, and is applied to all elements (regardless of their physical group).
- `NodalMass` boundary condition which distributes a non-structural mass over the nodes belonging to a certain physical group.
- `ModalPrestressed` analysis type, which takes care of a linear static analysis to determine the equilibrium state of a system, followed by a modal analysis that computes the eigenfrequencies and modes. An important feature of this class is that it keeps track of the material and geometric contributions to the tangent stiffness matrix, which is important for optimization purposes.

Optimization Framework Adjustments

- The way in which `Step.assemble()` does matrix assembly was adjusted to support using vectorized element assembly in combination with the `SparseMatrixRaw` format. This was done to allow for the use of *all* vectorized elements in Topology Optimization. Previously only elements that were assembled in a non-vectorized way were supported.
- Support for `Step.assemble()` to assemble elements in a vectorized manner, *when different physical groups were present in the mesh* was added. This was implemented by making sure that vectorized assembly only assembles the elements belonging to a specific physical group, whilst looping over the groups present. In the context of optimization, this allows for physical groups of fixed density to be present inside the domain.
- Added support for TO density interpolation (which is done in `Design.applyInterpolation()`) for *multi-step problems*, with different matrices per problem. For example, in `ModalPrestressed` analysis the static step only requires the interpolation to be applied to $\boldsymbol{K}$ and $\boldsymbol{f}_\sigma$, whereas the subsequent modal step also requires interpolation to be applied to $\boldsymbol{G}$ and $\boldsymbol{M}$.
- Applying different penalizations to different system matrices is now supported. This can be added by supplying an optional `PenalizationDict`, which couples a `SensitivityFlag` to an interpolation function. The "standard" penalization (defined in the `*functions` argument in the`Design` object's initialization) is applied by default to all matrices not specified in this dictionary.
- Adjusted `MMA.py` to support multiple constraints.
- Adjusted `StijnsMMA.py` work with density-based TO problems.

- Added method to `SparseMatrixRaw` to extract a single element based on element ID.
- Added a method in `SparseMatrixRaw` to re-order the datastructures based on a desired list of element IDs. This is necessary when working with raw matrix format, in combination with multiple physical groups. In a sample case that has 3 elements and two groups, element [2] can be in group 1 and elements [1,3] can be in group 2. As the assembly is done in *ascending group order*, this will result in a [2,1,3] ordering in the `SparseMatrixRaw` data structure. This applies the wrong density to to elements 1 and 2 (density of 1 is applied to 2 and vice versa). This is because the elements in each group are assembled in ascending order of the group key, but this does not guarantee ascending order of element ID. The ascending IDs are import for applying the correct density to each element in `ScaleVisitor.applyInterpolation()`, as the densities are stored/applied in *ascending* element order. A check was added to `Step.assemble()` to ensure that matrices resulting from vectorized raw assembly are in ascending order by element ID, and it calls the new method to re-order them if necessary (This bug took quite some time to find).

Optimization Objectives, Constraints & Sensitivities

- Objective: added `Eigenfrequency` for `Modal` steps.
- Objective: added `PrestressedEigenfrequency` for `PrestressedModal` steps.
- Objective: added `QratioAdjoint` and `QratioNelson`, to maximize the Q-factor ratio explained in this thesis. Note that the second method is very slow, as it involves computing the derivative of the mode shape with respect to the design density. The first method omits this computation. The slow second method uses a novel trick of Lagrange multiplier matrices, as described in the "second" manuscript in this thesis.
- Constraint: added `FrequencyConstraint` and `QratioConstraint`, which adds a lower or upper bound for a specific eigenfrequency or dilution factor.
- Constraint: added `FrequencyRatioConstraint`, which adds a lower or upper bound for a ratio of frequencies. If a certain ratio is desired, then two of these constraints should be added (one with an upper and one with a lower bound).
- `VolumeConstraint` now supports meshes with non-uniform element sizes, as well as fixed density regions within the mesh.
- After doing a Finite Difference check, the unperturbed design is now saved to the output instead of the final perturbed design.
- Added support for applying a projection function on top of the filtered densities. As this influences the computation of constraints and objectives (through the chain rule), implementing this feature was not trivial. By default, an `IdentityProjection` is now applied to all problems (which serves as a placeholder).
- The sensitivity of a constraint can now be checked with Finite Differences, by using the new `ConstraintAsObjective`. This object mimics an input constraint and enables it to be used as an objective. It is useful to verify whether newly added constraints have been implemented correctly. Correct application of the chain rule should be kept in mind when testing constraint functions with finite differencing, as it could be that e.g. the filtering derivative is taken into account twice (see the note in the `VolumeConstraint` code).
- Extra feature of static displacement interpolation added to `ModalPrestressed`, to reduce wrinkling instabilities. This is also taken into account in the sensitivity analysis (this was also not straightforward to implement).
- Implemented the Robust formulation for TO problems. This uses the existing TO framework, with `Robust_Formulation` as the analysis, `Robust_Objective` as the objective wrapper and `Robust_Constraint` as the constraint wrapper. For one set of design variables the problem is solved using three projection thresholds. The worst-performing design is subsequently chosen to optimize for. During the optimization, the projection slope is slowly increased. This helps to arrive at fully black-and-white designs, and control length scales in the final design. Importantly, the implementation keeps track of all designs and sensitivities, and uses the appropriate one for the objective/constraint sen-

sitivity analysis. This methodology is recommended for TO problems that aim to maximize the Q factor.

Other Optimization Features

- New material interpolation functions: `FixedDiffSimp` and `LinearDiffSIMP` can be used to prevent modes in low-density regions in TO.
- Added Young's modulus minimumm ratio to the `RAMP` interpolation function (to ensure void/material stiffness ratio becomes independent of minimum density).
- Added `TanhProjection`
- Added `LinearMassInterpolation` to be applied to the mass matrix in modal problems, with a minimum mass ratio (to ensure void/material mass ratio becomes independent of minimum density).
- `UpdateVariableConvergence` is a new type of convergence, which updates a certain parameter once an intermediate design converges. The intermediate convergence check can be either based on the Design or Relative Difference. The parameter to update is determined by supplying the penalization/projection function in the initialization of this convergence object. This function must have a method named `updateVariable()`.
- `UpdateVariableIterations` is similar to `UpdateVariableConvergence`, but allows the user to set a predefined number of iterations per variable.
- A new `Tester` class can be used to analyze the performance of a given design vector or design object.
- The `Optimization` class can now print its iterations, objectives and constraint values to the console once the problems has been solved. This functionality was also made available for Level-Set based optimization studies.
- An interesting method named `AnalyzeConvexity` was added as an experiment to the `Optimization` object. This perturbs the design along two vectors and turns this into 2D map. This was not look into much due to time constraints, in addition to the non-convexity added by the sigmoid/logit functions (which were needed to keep the densities between d_{min} and 1).

Plotting Features

- A method that turns a list of ParaView output files into a GIF was added to `io/VTK.py`. This makes use of the `pyvista` package.
- 3D surface plots can be made from `io/Matplot`.
- Plotting the relative difference as a function of stepsize (in FD checks) was added.
- `Optimization` objects can be initialized with `PlotFlags`. These indicate quantities to compute during each optimization run, and are automatically plotted at the end. The available flags are listed in `definitions.py`, and the computation of each flag occurs in `Optimization.computePlotFlags()`. A directory can be supplied to save the plots in. This is a very useful functionality when doing lots of simulations, as the objectives an constraints as a function of the iteration number can easily be plotted and saved automatically. Flags are computed uniquely to save computational time (in case a flag is required for multiple plots).

Wishlist

- Loading and analyzing designs from ParaView files.
- Automatically saving certain parameters as txt files at the end of an optimization study (should be relatively easy to implement).

C

Guide to Working with Hybrida on Windows

In this project, the Anaconda distribution of Python was used on Windows. This chapter gives a quick overview of how Hybrida can be set up.

Setting Up a Virtual Environment

A virtual environment must be created. Within this environment, specific versions of Python itself as well as several packages (e.g., numpy, scipy ect.) are installed with which Hybrida is known to be compatible. Anaconda has an accessible built-in way to manage virtual environments.

- Download and install Anaconda from www.anaconda.com.
- Launch the Anaconda Navigator and open the CMD.exe prompt.
- Create a new virtual environment using the following command:
  `conda create --name NAME python=3.10.6`
  A custom name can be filled into "NAME", and the preferred version of Python is given at the end. In this project, 3.10.6 was used. You have now created a new virtual environment with a specific version of Python.

Setting up Hybrida without GitLab

- Download Hybrida from the repository. Unzip the file and place it somewhere you can find it on your computer.
- In Anaconda Navigator, change the current environment to the new environment you previously created. This can be done from the home page, where the default option is named 'base (root)'. If the command window from setting up the previous environment is still open, it is also possible just to use the following command:
  `conda activate NAME`
- In a command prompt with the correct virtual environment loaded (the environment name should be shown between parentheses), change the directory to the Hybrida master folder (i.e., the folder previously downloaded from the repository).
- Use the following command to install the required packages and dependencies:
  `pip install -r requirements.txt`

Working with Gitlab

The following sequence of command should be used when pushing changes made to the repository. These commands should be done in the directory of your `Hybrida` folder, and only make sense if you have set it up by cloning from the repository using git directly.

- you need to commit first your changes locally, so you do:
  `git status` (to see the status of files added/removed/etc.)
- `git add .` (at the top of the hierarchy, to add/remove files)
- `git commit -m "- Add a descriptive message of the commit"` (this will commit the files locally)
- `git pull` (this will pull the changes from the repository)
- `python -m pytest -v tests/ examples/` (check how many tests are failing on your computer)

This last step is important because it will tell you whether your implementation broke any tests. If you have broken something, you need to fix it before you push the changes to the repository. Afterwards, repeat the follwing sequence:

- `git status`
- `git add .`
- `git commit -m "- Add a descriptive message of the commit"`
- `git push`